Journal of the Meteorological Society of Japan

EARLY ONLINE RELEASE

The DOI for this manuscript is
DOI:10.2151/jmsj.2021-073
J-STAGE Advance published date: September 1st, 2021
The final manuscript after publication will replace the preliminary version at the above DOI once it is available.

Different Future Changes between Early and Late Summer Monsoon Precipitation in East Asia

Hirokazu ENDO[1], Akio KITOH[2,1], Ryo MIZUTA[1]

and

Tomoaki OSE[1]

1) Meteorological Research Institute, Tsukuba, Japan
2) Japan Meteorological Business Support Center, Tsukuba, Japan

Version 1: November 30, 2020
Version 2: May 31, 2021
Version 3: August 5, 2021
Version 3.1: August 16, 2021

Corresponding author: Hirokazu Endo, Meteorological Research Institute, 1-1 Nagamine, Tsukuba, Ibaraki 305-0052, JAPAN.
E-mail: hendo@mri-jma.go.jp
Tel: +81-29-853-8597

Abstract

Future changes in East Asian summer monsoon (EASM) precipitation and the associated atmospheric circulation changes are investigated based on ensemble projections with the 60-km mesh Meteorological Research Institute atmospheric general circulation model (MRI-AGCM60). The projections at the end of the twenty-first century under the Representative Concentration Pathway 8.5 (RCP8.5) scenario indicate an overall increase in EASM precipitation, but with large sub-seasonal and regional variations. In June, the Meiyu–Baiu rainband is projected to strengthen, with its eastern part (i.e., the Baiu rainband) shifted southward relative to its present-day position. This result is robust within the ensemble simulations. In July and August, the simulations consistently project a significant increase in precipitation over the northern East Asian continent and neighboring seas; however, there is a lack of consensus on the projection of the Meiyu–Baiu rainband in July. A small change in precipitation over the Pacific is another feature in August.

Sensitivity experiments with the MRI-AGCM60 reveal that the precipitation changes in early summer are dominated by the effects of sea surface temperature (SST) warming (i.e., uniform warming and the tropical pattern change), which induce an increase in atmospheric moisture and a strengthening and southward shift of the upper-level East Asian westerly jet (EAJ), especially over the Pacific. On the other hand, the influence of land warming and successive large SST warming in the extratropics is evident in the precipitation changes in late summer. These late summer effects oppose and exceed the early summer effects through changes in the EAJ and low-level monsoon winds. These results suggest that the competition between the opposing factors makes the signal of the Meiyu–Baiu rainband response smaller in July than in June, and thus there tends to be a larger spread among simulations regarding the future tendency of the rainband in July.

Keywords summer monsoon; East Asia; global warming; Baiu; MRI-AGCM

1. Introduction

The East Asian summer monsoon (EASM) that affects eastern China, Korea, and Japan is a subsystem of the Asian summer monsoon. One of the prominent features of the EASM is the concentration of rainfall in a zonal rain belt, referred to as the Meiyu–Baiu rainband, which extends from eastern China to southern Japan (Wang et al. 2008). The Meiyu–Baiu rainband migrates northward in early summer, causing heavy precipitation and resultant natural disasters such as floods (Wang and LinHo 2002; Ninomiya 2004). The rainband is anchored by the East Asian westerly jet (EAJ) in the mid-to-upper troposphere and is supplied with abundant moisture by low-level southerly monsoonal winds blowing between the Asian continent and the Pacific Ocean (Kodama 1993; Sampe and Xie 2010). Around mid to late July, the Meiyu–Baiu rainband becomes weak, accompanied by a northward shift and weakening of the EAJ, while monsoon precipitation advances to northern China (Ding 2004; Suzuki and Hoskins 2009; Sampe and Xie 2010).

Global warming projections with coupled atmosphere–ocean general circulation models (AOGCMs) in the Coupled Model Intercomparison Project (CMIP) have shown that EASM precipitation is likely to increase (Kimoto 2005; Kitoh et al. 2013; Ha et al. 2020; Wang et al. 2020), following the "wet-gets-wetter" response via an increase in atmospheric moisture content and its transport in a warmer climate (Held and Soden 2006; Endo and Kitoh 2014). However, the spatial pattern of EASM precipitation changes have large uncertainties due to inter-model differences in regional atmospheric circulation changes (Zhou et al. 2018; Ito et al. 2020; Ose et al. 2020).

High-resolution atmospheric general circulation models (AGCMs) developed at the Meteorological Research Institute (MRI) have been applied to study regional climate change using a time-slice method, which prescribes the SST anomalies simulated by AOGCMs. Advantages of this approach include not only the realistic representation of local climatological features and small-scale processes, such as convective precipitation, but also the reduction of large systematic biases that originate from the sea surface temperature (SST) bias in the AOGCM climatology, enabling us to obtain reliable regional climate information (Kitoh et al. 2016). On the other hand, a weakness of this approach is that AGCMs do not represent the atmosphere–ocean interaction process, which may be important for realistically simulating Asian monsoon-related phenomena (e.g., Wang et al. 2005). Nevertheless, it has been documented that the high-resolution MRI-AGCM performs quite well in reproducing the climatology and extremes of EASM precipitation, as well as the seasonal northward migration of the Meiyu–Baiu rainband (Kitoh and Kusunoki 2008; Endo et al. 2017; Kusunoki 2018a; Chen et al. 2019).

A series of global warming experiments with the 20-km and 60-km mesh MRI-AGCMs have consistently projected an overall increase in the amount and intensity of EASM precipitation (Kitoh 2017). However, there exists large uncertainty in the spatial distribution of precipitation changes and in the seasonal march of the rainy season, both of which depend on the model version, the adopted cumulus convection schemes, and future SST pattern changes (Endo et al. 2012; Kusunoki 2018b; Ose 2019a). For example, earlier studies with the MRI-AGCM detected a delaying trend in the retreat of the rainy season in the vicinity of Japan (Kusunoki et al. 2006, 2011), whereas more recent simulations show unclear signals in the timing of the retreat (Kusunoki 2018b). Ose (2019a) indicated an important role of atmospheric circulation changes for characterizing the EASM precipitation distribution.

The total effects of increased CO_2 can be separated into the effect of direct CO_2 radiative forcing and the indirect SST-mediated effect. These correspond to different time scales of the response to an abrupt CO_2 increase in an AOGCM, and thus the former (latter) is often called the "fast response" ("slow response"; e.g., Bony et al. 2013). The direct CO_2 effect involves both direct atmospheric heating and subsequent land warming, whereas the indirect effect is associated with SST warming in response to increased CO_2. AGCM experiments based on this type of separation have been widely performed, providing useful insights into the mechanisms behind the global warming response (e.g., Tokioka and Saito 1992; Bony et al. 2013; Kamae et al. 2014; Shaw and Voigt 2015; Chen and Bordoni 2016; Chadwick et al. 2017; Li and Ting 2017; Endo et al. 2018; Qu and Huang 2020; Allan et al. 2020). For instance, Kamae et al. (2014) showed that future intensification of the land–sea surface-air-temperature (SAT) contrast in East Asia is explained primarily by land warming induced by the direct CO_2 forcing. Li and Ting (2017) revealed that the Asian summer monsoon precipitation change is dominated by the direct CO_2 effect through enhanced monsoon circulation. Endo et al. (2018) found that land warming induced by the direct CO_2 effect increases the land–sea thermal contrast in the lower troposphere, whereas upper-tropospheric warming in the tropics induced by SST warming decreases the land–sea contrast in the upper troposphere. These two effects therefore act in opposing ways on monsoon circulation and precipitation.

In this paper, we investigate future changes in EASM precipitation and the associated atmospheric circulation changes based on ensemble experiments with the 60-km mesh MRI-AGCM (MRI-AGCM60). We consider a large sub-seasonal variation of East Asian summer climate and conduct our analysis on a monthly basis. CMIP5 AOGCM projections are also analyzed to support our results. Furthermore, we perform sensitivity experiments with the MRI-AGCM60 to understand the relative roles of the direct greenhouse-gas (GHG)-induced land warming and the SST warming, as well as the SST pattern changes in the future.

2. Models and experiments

2.1 MRI-AGCM60

The model used in this study is the MRI-AGCM version 3.2 (Mizuta et al. 2012), which is run at a horizontal resolution of TL319 (corresponding approximately to a 60-km-mesh grid). The model has 60 vertical levels, with the model top at 0.01 hPa. The cumulus convection parameterization scheme used in the model is chosen from one of three types: the

Yoshimura (YS) convection scheme (Yoshimura et al. 2015) as the default, the Arakawa-Schubert convection scheme (AS; Randall and Pan 1993) modified by the Japan Meteorological Agency, and the Kain-Fritsch convection scheme (KF; Kain and Fritsch 1990). Previous studies indicated that precipitation changes in East Asia are sensitive to the cumulus convection scheme implemented in the model (Endo et al. 2012; Kusunoki 2018b).

2.2 Ensemble projections

Atmospheric Model Intercomparison Project (AMIP)-type time-slice simulations were conducted with the MRI-AGCM60. Two sets of ensemble projections were performed in order to cover a wide range of model uncertainties.

a. Multi-SST ensemble

The first ensemble contains multi-SST projections (Table 1). For the present-day simulation (1979–2003), observed interannually-varying monthly SST and sea ice concentration (SIC) data from HadISST1.1 (Rayner et al. 2003) were used as the boundary conditions. Ensemble runs consisting of two members were conducted with different atmospheric initial conditions.

For the future simulation (2075–2099), 28 different SST warming patterns obtained from each CMIP5 model projection under the Representative Concentration Pathway 8.5 (RCP8.5) scenario were used (Fig. S1). The future SSTs were created using the method of Mizuta et al. (2008), where they are calculated as the sum of the observed SST and CMIP5 model-projected SST anomalies, and the interannual SST variability in the future is assumed to be the same as in the present day. Here, note that the future SST anomalies are different from month to month, and that they are scaled so that their annual tropical (30°S–30°N) mean has the same value as the CMIP5 multi-model mean (i.e., 2.74 K) (Mizuta et al. 2014). The future SICs were created by the method of Mizuta et al. (2008), where the CMIP5 model-mean anomaly is used.

b. Multi-physics and multi-SST ensemble

The second ensemble contains the multi-physics and multi-SST projections (Table 2). For the present-day simulation (1984–2003), ensemble simulations combining three different types of cumulus convection parameterization schemes (i.e., YS, AS, and KF) with two different atmospheric initial conditions were performed.

For the future simulation (2080–2099), ensemble simulations combining three different types of cumulus convection parameterization schemes (i.e., YS, AS, and KF) with four different SST warming patterns from the CMIP5 projections under the RCP8.5 scenario were performed. The future SSTs and SICs were created using the method of Mizuta et al. (2008), where the CMIP5 model-mean anomaly (the models selected here are the same as those in the multi-SST ensemble projections) and three different SST/SIC anomalies derived from a cluster analysis of the CMIP5 projections are used (Fig. S2; Mizuta et al. 2014).

2.3 Sensitivity experiments

To understand the mechanisms behind the projected changes, additional experiments were performed using the MRI-AGCM60 (Table 3). In these experiments, we use the YS convection scheme, because the model with the YS scheme has the highest performance in simulating the precipitation distribution over the globe among the YS, KF, and AS schemes (Kusunoki 2017). As a result, it has been extensively utilized as the standard scheme of the MRI-AGCM for global warming projections, such as in simulations with a 20-km-mesh (e.g., Kusunoki 2018b), as well as with a large number of ensemble members (Mizuta et al. 2017). The runs denoted ‘HP’ in Table 3 are the present-day simulations and include the HP01 and HP02 runs in Table 1. The runs denoted ‘HF’ in Table 3 are the future scenario simulations using the CMIP5 multi-model mean SST anomaly and are the same as the HFYSC0 run in Table 2, except for the simulation period. Hereafter, the HF minus HP is denoted as ‘ALL’, which means the response to all forcing.

In addition to these conventional experiments, AMIP-type sensitivity experiments (Exp1–Exp4 in Table 3) were conducted, where either GHG concentrations or SSTs were modified as follows: (1) Exp1: GHG concentrations are increased without changing SST; (2) Exp2: SST is uniformly increased by 2.74 K without changing any other forcing; (3) Exp3: The future SST anomaly is used, except in the tropics (30°S–30°N) where SST is uniformly increased by 2.74 K; (4) Exp4: The future SST anomaly is used, except in the Northern Hemisphere (NH) extra-tropics (30°N–90°N) where SST is uniformly increased by 2.74 K. We note that the uniform SST warming of 2.74 K corresponds to the tropical-averaged SST change between the HF and HP runs (Mizuta et al. 2014), and that the boundaries between the tropics and the extratropics for the SST anomaly data have linear tapering zones over 27.5°N–32.5°N and 27.5°S–32.5°S.

Using these experiments, the following four factors are isolated: (1) direct GHG radiative forcing (Exp1 minus HP; GHGrad); (2) globally uniform SST warming (Exp2 minus HP; SSTunif); (3) SST pattern change in the tropics (30°S–30°N; HF minus Exp3; SSTtp); and (4) SST pattern change in the NH extratropics (HF minus Exp4; SSTnh). These types of AGCM experiment (i.e., separating the total response into the fast response associated with GHG radiative forcing and the slow response associated with SST warming) have been conducted extensively, as described in the Introduction. In our experiments, the slow response of the SST warming is further divided into three parts (factors 2–4 mentioned above) to isolate the effect of globally uniform SST warming, as well as SST pattern changes in the tropics and extratropics.

2.4 CMIP5 AOGCMs

The projections with the MRI-AGCM60 were compared with the CMIP5 AOGCM projections. The 28 CMIP5 models analyzed are the same as those used to create the future SST anomalies in the multi-SST ensemble projections (Section 2.2.a), as well as in the multi-physics and multi-SST ensemble projections (Section 2.2.b). Results from the historical (1979–2003) and RCP8.5 scenario (2075–2099) experiments were investigated. All model outputs were re-gridded onto a 2.5° longitude by 2.5° latitude mesh, and their future changes were scaled by the CMIP5 model-mean SST anomaly over the tropics (i.e., 2.74 K) before being averaged across models to make the multi-model mean.

3. **Present-day climate simulation**

Figure 1 shows the mean precipitation, sea-level pressure (SLP), and zonal wind at 300 hPa (U300) from June to August (JJA) based on observations and the present-day climate simulations. In observations (Figs. 1a–d), the pronounced Meiyu–Baiu rainband extends from southeastern China to southern Japan in June. The western North Pacific subtropical high (WNPSH) expands westward to the south of the rainband, while the EAJ in the upper troposphere lies north of the rainband. The WNPSH and EAJ migrate northward with as the seasonal progresses. In July, the intensity of the rainband and EAJ becomes weaker and the wet area advances into northern China. In August, the EAJ reaches its highest latitude with a slightly stronger intensity than that in July, and the WNPSH expands northwestward and dominates over Japan.

The seasonal northward migration of the Meiyu–Baiu rainband is a unique feature of the East Asian summer climate. It is well documented that the upper-level EAJ is an essential environmental factor for the existence of the pronounced rainband and its seasonal migration (e.g., Kodama 1993). Sampe and Xie (2010) revealed that the EAJ anchors the Meiyu–Baiu rainband by advecting warm air from the continent in the mid-troposphere to induce adiabatic upward motion, and also by guiding transient disturbances. Horinouchi and Hayashi (2017) suggested that the interaction between the upper-level EAJ and low-level jet plays a significant role in enhancing the rainband.

The large-scale features of the spatial distribution and seasonal march are well simulated by the MRI-AGCM60 (Figs. 1e–l), but there are biases, such as a weaker Meiyu–Baiu rainband in June, as well as a slightly stronger and southward-biased westerly jet during July and August. The CMIP5 multi-model mean also reproduces the observed features in general; however, some biases are noted, including poor representation of the rainband, an insufficient meridional contrast of precipitation distribution over China, especially in June, and a weaker westerly jet throughout the summer (Figs. 1m–p).

4. Ensemble projections with the MRI-AGCM60

Future precipitation changes in the multi-SST ensemble (hereafter SST ensemble) and the multi-physics and multi-SST (hereafter physics-SST ensemble) with the MRI-AGCM60 are shown in Figs. 2a–d and 2e–h, respectively. For the JJA mean, both the ensembles project an increase in precipitation over most of East Asia. The area-averaged precipitation over the East Asian land region (EAS; 20°N–50°N, 100°E–145°E), defined in IPCC (2013), is projected to increase for all members. However, some areas show a negative change, such as in the vicinity of Japan.

On a monthly basis, there are distinct spatial and temporal variations in the precipitation change. In June, the Meiyu–Baiu rainband is projected to strengthen, with its eastern part (i.e., the Baiu rainband) remaining south of the present-day position and a relatively drier zone to the north of the rainband. These features are common to both ensemble projections, with high agreement among members, indicating that the result is robust. In July and August, the simulations consistently project a significant increase in precipitation over the northern East Asian continent and the neighboring seas, including the Yellow Sea and the Sea of Japan, with the highest increase over the continent in July (though a precipitation increase in the northern East Asian continent is seen in June as well). These robust features can also be observed when the robustness is measured in a different way, where the future changes are normalized by the inter-member (or inter-model) standard deviation of the changes (Fig. S2). On the other hand, there is a lack of consensus in the projection of the Meiyu–Baiu rainband in July, since the SST ensemble projects a northward shift and weakening of the rainband, while the physics-SST ensemble projects an intensification of the rainband at the present-day position. A small change in precipitation over the Pacific is another feature in August. Ose (2019a) compared future projections with the YS, KF, and AS schemes, and noted that the qualitative difference in July is attributed to the YS model.

The main features of the MRI-AGCM60 projections described above are similar to the CMIP5 AOGCM projections, especially when focusing on the hatched areas (Fig. 2i–l). The similarity between the ensembles becomes more visible when 10 good CMIP5 models are chosen based on a metric to evaluate their present-day simulations (fig. 3 of Ose (2019b)).

However, there are some disagreements between the ensembles: in June, the MRI-AGCM60 consistently projects an intensification of the Meiyu rainband, despite there being no robust signal in the CMIP5 projection; in July, although there is no consensus in the MRI-AGCM60 ensemble projections, the major CMIP5 models project that the Baiu rainband will stay around southern Japan.

Figure 3 shows future changes in SLP, 850-hPa wind, and U300. In June, negative SLP anomalies prevail over East Asia, indicating an overall weakening of the WNPSH. Over the Pacific, there are northerly wind anomalies at 850 hPa and a slight southward shift of the EAJ at 300 hPa. In July and August, the EAJ is projected to be weaker, especially over the Pacific. In the lower troposphere, the southerly monsoon wind strengthens over the East Asian continent, while northerly wind anomalies prevail over the Pacific, in a broadly consistent manner to the CMIP5 model-mean response. The WNPSH intensifies near the continent in the subtropics and contracts southward over the Pacific. These features indicate an east–west difference in the low-level circulation change. The MRI-AGCM60 tends to project a stronger WNPSH compared with the CMIP5 multi-model average. Based on a CMIP5 multi-model analysis, Ose et al. (2020) demonstrated that the strength of the future WNPSH is a primary uncertainty in the projection of East Asian SLP in JJA and is strongly correlated with future changes to the upper-level EAJ.

Figure 4 illustrates the time–latitude cross-section of future changes in precipitation and U300 in the vicinity of Japan (averaged over 125°E–145°E). The overall features of their changes are broadly similar among the three ensembles. For example, precipitation is generally projected to increase during warm seasons in the 25°N–40°N zone, and to increase throughout the year at latitudes higher than 40°N. In early summer, the rainband over Japan, corresponding to the Baiu rainband, is projected to strengthen and shift southward, as noted from Fig. 2. The upper-level EAJ shows a strong seasonal dependence: the EAJ shifts northward during cold seasons, but southward in early summer, followed by its overall weakening in late summer to early autumn. Thus, there exists a difference in the EAJ response between early summer and the following seasons, but with a slight difference between the ensembles in the timing of the termination of the early summer response.

Previous studies have shown that the seasonal northward migration of the Baiu rainband will be delayed in future, although some uncertainty exists in the results (Kusunoki 2018b). Based on a CMIP multi-model analysis, Hirahara et al. (2012) and Horinouchi et al. (2019) pointed out that this is associated with a southward shift of the EAJ in early summer. The MRI-AGCM60 ensemble projections are generally consistent with these previous studies. However, our detailed analysis throughout the summer season reveals that the EAJ response has different features between early and late summer; namely, a southward shift in early summer with an overall weakening in late summer.

5. Sensitivity experiments with the MRI-AGCM60

In this section, we investigate the mechanisms behind the projected future changes in precipitation and the associated atmospheric circulation based on sensitivity experiments (Table 3), focusing on their differences between early and late summer. We first discuss the responses on a global scale (Section 5.1) before concentrating on East Asia (Section 5.2).

5.1 Global aspects

Figure 5 shows the responses in June for SAT, precipitation, and zonal wind at 200 hPa, and those for SLP and vertical velocity at 500 hPa are given in Fig. S4. The response to ALL (i.e., HF minus HP) shows a greater increase in SAT over land than over ocean, with larger SAT increases at high latitudes (Fig. 5a). The precipitation change is generally explained by a combination of the "wet-gets-wetter and dry-gets-drier" pattern (Held and Soden 2006) and the "warmer-gets-wetter and colder-gets-drier" pattern (Xie et al. 2010), as described later (Fig. 5f). The upper-level subtropical westerly jet is projected to shift southward over southern Asia to the North Pacific, but northward over the North Atlantic (Fig. 5k).

The GHGrad effect involves both direct atmospheric heating and associated land warming, with the former causing a small increase in static stability in the lower troposphere and the latter enhancing the land–sea SAT contrast, especially over the NH extratropics (Fig. 5b; He and Soden 2015; Chadwick et al. 2019). The future intensification of the land–sea SAT contrast in East Asia is primarily attributed to the GHGrad effect (Kamae et al. 2014). The resultant increase in the land–sea pressure gradient strengthens moisture convergence and precipitation over land (Figs. 5g, S4b, and S4g). These responses are accompanied by a weakening and poleward shift of the subtropical jet over southern Asia to the North Pacific

(Fig. 5l), as noted by Shaw and Voigt (2015) and Endo et al. (2018).

The SSTunif leads to atmospheric moisture build-up, resulting in a general increase (decrease) in precipitation over wet (dry) regions in the present-day through an intensification of moisture transport (Fig. 5h). This is typically referred to as the “wet-gets-wetter and dry-gets-drier” response (Held and Soden 2006). This thermodynamic change is partly offset by a weakening of the atmospheric vertical motion, due to increased static stability of the troposphere (Fig. S4h; Held and Soden 2006; Chadwick et al. 2013). In contrast to the case of GHGrad, the SSTunif decreases the land–sea thermal contrast, especially in the upper troposphere, but not near the surface in low-latitude dry regions (Fig. 5c; Endo et al. 2018). This makes the monsoon circulation weaker through a decrease in the pressure gradient (Fig. S4c), resulting in a general spatial shift of the precipitation distribution from land to ocean (Fig. 5h; Chadwick 2016). These responses are accompanied by a strengthening and southward shift of the subtropical westerly jet over southern Asia to the North Pacific, exhibiting a close resemblance to the response to ALL (Figs. 5k and 5m).

The SSTtp influence on precipitation is known as the “warmer-gets-wetter and colder-gets-dryer” response; that is, tropical precipitation tends to increase (decrease) over areas where the SST change is higher (lower) than the tropical mean, due to changes in local convective instability (Xie et al. 2010). For example, atmospheric convection increases over the equatorial Pacific and the western-to-central Indian Ocean and decreases over the northwestern Pacific, the surroundings of the Maritime Continent, and the Caribbean Sea following the relative SST change (Figs. 5i and S4i). As a result of the convection changes, the WNPSH becomes weaker and the upper-level subtropical jet shifts southward over southern Asia to the North Pacific (Figs. 5n and S4d).

The response to SSTnh is characterized by large SAT warming in the NH extratropics, especially in the mid-latitudes of the North Pacific (Fig. 5e). The prominent warming over the North Pacific occurs mainly in late summer to early autumn, as shown later. There is no significant change in either the precipitation or atmospheric circulation fields in response to the SSTnh in June (Figs. 5j and 5o).

Figures 6 and S5 show the responses in August. Compared with those in June, the general features of the response are similar, but some differences are noted. More prominent SAT warming is seen in the NH extratropics in August than in June (Fig. 6a). This comes from a larger land warming in response to the GHGrad, and a greater SST warming in the NH extratropics, especially over the North Pacific (Figs. 6b and 6e). The SSTnh exerts significant influence on the precipitation and atmospheric circulation in August, including a strong response of the upper-level EAJ (Figs. 6e, 6j, 6o, S5e, and S5j).

In order to measure the similarity between the future changes with ALL and with each individual factor isolated from the sensitivity experiments (i.e., GHGrad, SSTunif, SSTtp, and SSTnh), the spatial correlation coefficients between them are calculated over the area 0°E–360°E, 20°S–80°N for several atmospheric variables (Fig. 7). In June, the SSTunif and SSTtp tend to have higher correlation coefficients with ALL in precipitation and atmospheric circulation variables than the other factors. In July and August, however, the correlation of the GHGrad and SSTnh with ALL become high and are comparable with those of the SSTunif and SSTtp in most variables, suggesting that the importance of the four factors to ALL vary between early and late summer. The same features are also seen in East Asia, but the monthly dependence is even stronger (Fig. 8): the response to ALL is similar to the SSTunif and SSTtp (GHGrad and SSTnh) in many variables in June (July and August). Shaw and Voigt (2015) identified a weak response of the Asian monsoon circulation and of the westerly jet over the North Pacific in the JJA mean field in future climate due to the GHG radiative forcing and SST warming responses compensating one another. However, our results indicate that the signal of atmospheric circulation change is not small when considered on a monthly basis, and that the balance of the factors contributing to the total response varies between early and late summer, especially in East Asia.

5.2 East Asia

The summertime precipitation responses in East Asia are shown in Fig. 9, and their time-latitude cross-sections averaged over 125°E–145°E are presented in Fig. 10. There is a close similarity between the MRI-AGCM60 projections forced by the CMIP5 model-mean future SST anomaly (Figs. 9a–d and 10a) and the average of the SST-ensemble projections (Figs. 2a–d and 4a) forced by different SST anomalies from each CMIP5 model, suggesting an almost linear response of precipitation to the prescribed SST anomalies. The sum of the four factors derived from the sensitivity experiments (Figs. 9e–h and 10b) reproduces the response to ALL well (Figs. 9a–d and 10a), giving justification to our approach to isolate each mechanism. As mentioned in Section 4, the EASM precipitation is projected to increase overall, but with large temporal and spatial variations. Monthly precipitation changes are characterized by an intensification of the Meiyu–Baiu rainband with its eastern part shifted southward in June, as well as a significant increase in precipitation over the northern East Asian continent and the neighboring seas in July and August. A small change in precipitation over the Pacific is another feature in August (Figs 9a–d and 10a).

The sensitivity experiments reveal that, although the projected overall increase in EASM precipitation is mainly attributable to the combined effects of GHGrad and SSTunif, all of the four factors studied contribute to the spatial pattern of the changes (Fig. 9). The SSTunif greatly enhances precipitation over oceanic regions, including Japan, during warm seasons, with a southward displacement of the Meiyu–Baiu rainband in June (Figs. 9m–p and 10d). The SSTtp shifts the rainband southward and activates it during warm seasons, especially in June (Figs. 9q–t and 10f). On the contrary, the GHGrad effect partly cancels the effects of the SSTunif and SSTtp through a shift of precipitation from ocean to land, accompanied by a northward shift of the rainband in June and its weakening in July (Figs. 9i–l and 10c). This corresponds to an earlier-than-normal seasonal march of the rainy season, driven by the enhanced land–sea thermal contrast, as discussed later. Moreover, the SSTnh leads to reduced precipitation in the vicinity of Japan in July and August, in contrast to increased precipitation over the continent and the Yellow Sea (Figs. 9u–x and 10e). Taking these four factors together, the early summer precipitation response is dominated by the effects of the SSTunif and SSTtp, whereas the effects of the GHGrad and SSTnh are influential in the late summer, resulting in a different precipitation response between early and late summer (Figs. 8–10).

We note that there is some convection-scheme dependence of the precipitation changes especially for the Meiyu–Baiu rainband in July. Specifically, the model with the YS scheme tends to project a weakening and northward seasonal migration of the rainband earlier than the model with other schemes (Figs. 2 and 4a–c). Thus, there may be some uncertainty in the balance between the four factors.

Figure 11 indicates summertime responses in SLP, 850-hPa wind, and U300 in East Asia. As in the precipitation response, the sum of the four factors is in accordance with the response to ALL in general (Figs. 11a–h). The sensitivity experiments reveal that the GHGrad strengthens the low-level EASM circulation, with the largest response in July, and induces a weakening and northward shift of the upper-level EAJ (Figs. 11i–l). In contrast, the SSTunif weakens the low-level EASM circulation, and it strengthens and shifts the EAJ southward, especially over the Pacific (Figs. 11m–p). These contrasting changes in circulation are explained by the opposite responses of the land–sea thermal contrast to the GHGrad and SSTunif (Shaw and Voigt 2015; Endo et al. 2018). The SSTtp induces a southwestward movement of the WNPSH, as well as low-level northerly wind anomalies over the Pacific, and brings an intensification and southward-shift of the EAJ (Figs. 11q–t). The SSTnh drives a low-level anticyclonic circulation anomaly over Japan in August, enhancing winds from ocean to land, with a weakened and northward-shifted EAJ (Fig. 11x). Although these four factors partially offset each other, the future responses in June are explained primarily by the effects of the SSTunif and SSTtp (Figs. 8 and 11a–d). However, the effects of the GHGrad and SSTnh become large in July and August, resulting in a weakened upper-level EAJ, with stronger low-level southwesterly monsoonal winds over the continent (Figs. 8 and 11).

The time–latitude cross-section of the U300 anomaly averaged over 125°E–145°E is displayed in Fig. 12. Future changes in the EAJ show a distinct seasonal variation, which is explained mostly by a combination of the four factors studied (Fig. 12a). Both the SSTunif and SSTtp strengthen and displace the EAJ southward during warm seasons and displace the EAJ northward during cold seasons (Figs 12d and 12f). In contrast, the GHGrad leads to a weakening and northward shift of the EAJ during warm seasons, especially in July and August (Fig. 12c), largely offsetting the SST warming effects. Moreover, the SSTnh reinforces the weakened and northward-shifted EAJ in late summer to early autumn (Figs 12e). In terms of the seasonal cycle, the SSTunif and SSTtp induce a weakening of the seasonality of the EAJ, while the GHGrad advances the seasonal progress from spring to summer, and the SSTnh extends the late (high) summer condition into early autumn. It is worth noting the difference between warm and cold seasons in response to the SSTunif.

The cold-season response may be associated with a northward shift of the storm track resulting from an increase in the upper-tropospheric meridional temperature gradient (MTG) and in subtropical atmospheric stability (Harvey et al. 2014), whereas the warm-season response, corresponding to a southward shift of the subtropical westerly jet, is probably influenced by a weakening of vertical motion over the tropics due to a stabilized atmosphere (Hirahara et al. 2012; Ose 2019b).

In relation to the precipitation response, the meridional displacement of the EAJ and the Baiu rainband appear to be closely related: a southward (northward) shift of the EAJ, induced by the effects of the SSTunif and SSTtp (GHGrad and SSTnh), is related to the southward-shifted (northward-shifted) rainband (Figs 9–12). Horinouchi et al. (2019) noted that future meridional shifts of the EAJ axis and Baiu precipitation peak latitudes are positively correlated across the CMIP5 models. In addition, the northward-shifted and weakened EAJ, associated with the GHGrad and SSTnh effects, seems to weaken the Baiu rainband intensity in late summer. This is similar to the situation occurring at the end of the Baiu season around mid-to-late July in climatology (e.g., Suzuki and Hoskins 2009). Sampe and Xie (2010) explained that the northward-shifted EAJ weakens warm advection from the continent because it flows north of the temperature maximum located south of the Tibetan Plateau, resulting in less upward motion that is needed to maintain the rainband.

Figure 13 presents the responses in tropospheric temperature averaged over 100°E–160°E. Both the GHGrad and SSTnh act to warm higher latitudes in summer, with the peak warming occurring around July–August and August–September, respectively. This reduces the MTG around Japan, causing a weakening of the EAJ through the thermal wind balance. This difference in the seasonality probably comes from the different characteristics of land and ocean. Specifically, the timing of the land (sea) surface warming-peaks for the GHGrad (SSTnh) roughly follows the seasonal maximum of its present-day climatology, with a lag of about one month for the SSTnh (Figs. 14b and 14c). Therefore, the emergence of the effects of GHGrad and SSTnh seems to be constrained by the seasonal cycles of land and sea surface temperature climatology, respectively, and thus they act to amplify the background seasonal cycle. There is a possibility that the land warming and successive SST warming in mid-latitudes are closely related to each other via land–atmosphere–ocean interactions, so that the pronounced mid-latitude warming is sustained until early autumn (Fig. 14a). Based on observational and CMIP5 model analysis, Santer et al. (2018) found that prominent mid-latitude warming occurs globally in boreal summer and is a robust signal of the human influence, noting that summertime continental drying may be a possible mechanism. Chen and Wang (2015) suggested that a decrease of mixed layer depth in summer in response to global warming is the main reason for the intensification of the SST annual cycle over the North Pacific.

Recent studies have shown that mid-latitude SST anomalies over the North Pacific have a significant impact on East Asian summer climate, such as the Baiu rainband, through modulation of the EAJ (Nakamura and Miyama 2014; Matsumura et al. 2016; Nishii et al.

2020). Based on a CMIP5 multi-model analysis, Matsumura et al. (2019) indicated that the SST gradient in the Kuroshio and Oyashio Extension (KOE) region will be weaker in future, especially in summer and autumn, and that there is a significant relationship across the models between a weakening of the KOE SST gradient and a weakening of the westerly jet over the western North Pacific. Our AGCM experiments indicate that the prominent SST warming in the NH extratropics induces a weakening and northward shift of the EAJ, with reduced precipitation around Japan in late summer, which is generally consistent with previous studies.

6. Summary and discussion

We investigated future changes in EASM precipitation and the associated atmospheric circulation changes at the end of the twenty-first century based on ensemble projections with the MRI-AGCM60, using different SST warming patterns and different types of cumulus convection schemes. The results indicate that EASM precipitation will increase overall, but there are large sub-seasonal and regional variations. In June, the Meiyu–Baiu rainband is projected to strengthen with its eastern part (i.e., the Baiu rainband) staying to the south of its present-day position. This feature is common not only to the MRI-AGCM60 ensemble projections, but also to the CMIP5 multi-model projections, suggesting that this change is robust. In July and August, a significant increase in precipitation is consistently projected over the northern East Asian continent and the neighboring seas, including the Yellow Sea and the Sea of Japan, with the highest increase over the continent in July. However, there is a large uncertainty in the projection of the Meiyu–Baiu rainband in July. A small change in precipitation over the Pacific is another feature in August.

Until now, future changes in summer precipitation in the vicinity of Japan have been explained primarily by thermodynamic and dynamic changes resulting from SST warming, including the tropical SST pattern change that was described as “El Niño-like” (Kitoh and Uchiyama 2006; Kusunoki et al. 2006; Hirahara et al. 2012; Inoue and Ueda 2012; Ogata et al. 2014). However, our sensitivity experiments with the MRI-AGCM60 reveal that land warming induced by direct greenhouse gas radiative forcing (GHGrad) and successive large SST warming in the extratropics (SSTnh) exerts a significant influence in late summer. These late summer effects oppose and exceed the effects of uniform SST warming (SSTunif) and the tropical SST pattern change (SSTtp) that work throughout the summer season, although there may be some uncertainty in the balance between the four factors.

The upper-level EAJ is influenced by the four factors studied and is related to the Baiu rainband activity. The SSTunif and SSTtp act to strengthen and displace the EAJ southward; in contrast, the GHGrad and SSTnh act to weaken and displace the EAJ northward, since they warm the mid-latitudes and reduce the MTG around Japan. Our sensitivity experiments show a positive relationship between the meridional displacement of the EAJ and the Baiu rainband. In addition, the northward-shifted and weakened EAJ, induced by the GHGrad and SSTnh, is associated with a weakening of the rainband in late summer. It is interesting to note that the SSTtp and SSTnh act in opposite ways on the responses of the EAJ around Japan. We also note that the weakening of the EAJ in late summer to early autumn have other implications for the future East Asian climate, including a slowdown of the translation speed of tropical cyclones in the mid-latitudes of the Pacific (Yamaguchi et al. 2020) and a possible effect on the autumnal rain over Japan.

In addition to the upper-level EAJ, low-level monsoon circulation is another important factor controlling EASM precipitation since it transports moisture from the tropics. The MRI-AGCM60 projects an intensification of southerly winds over the East Asian continent in July and August, in agreement with other global warming studies (e.g., He et al. 2019; Jin et al. 2020). This is mainly explained by the GHGrad and partly by the SSTnh effect. Note that the intensification of low-level monsoon winds probably results not only from an enhancement of the zonal land–sea temperature contrast, but also from a reduction of the MTG. The GHGrad and SSTnh weaken and displace the upper-level EAJ northward through a reduction of the MTG, resulting in a weakening of the Meiyu–Baiu rainband in late summer (e.g., Sampe and Xie 2010). This enables low-level monsoon winds to penetrate inland into northern China instead of weakened flow converging into the rainband over the ocean. This view is supported by previous studies suggesting that the EASM circulation is regulated by a combination of the zonal and meridional gradients in tropospheric temperature (Wang et al. 2008; Zhou and Zou 2010), and that variability of the low-level EASM circulation is closely coupled with the upper-level EAJ on annual and decadal time scales (Li et al. 2010; Zhou and Zou 2010; Song et al. 2014). Another feature of the future changes is northerly wind anomalies over the Pacific east of Japan during summer, which could be associated with a weakening of the subtropical anticyclone over the North Pacific (He et al. 2017). The sensitivity experiments indicate that the northerly wind anomalies come from the combined effect of the SSTunif, SSTtp, and SSTnh. Thus, the east–west contrast in the low-level circulation change is an important aspect of the late summer response in East Asia, which contributes to shaping the spatial pattern of the EASM precipitation changes (Ose, 2019a).

This study highlights a distinct difference between early and late summer in future changes of EASM precipitation. From early summer to late summer, the area with increased precipitation broadly moves from the ocean to the continent and neighboring seas. The first important factor of this is the "wet-get-wetter" response, which works to amplify the climatological spatial pattern of precipitation through an increase in moisture. The seasonal difference in the climatology (i.e., the active rainband over the ocean in early summer in contrast to active precipitation over and around the continent in late summer) contributes to the seasonality of the precipitation changes (Ose 2019a). Another important factor is the large differences in atmospheric circulation changes between early and late summer. According to the sensitivity experiments, the effects of land warming and prominent SST warming in the extratropics are enhanced in late summer, opposing and exceeding the effects of SST warming (i.e., uniform warming and the tropical pattern change) which work throughout the summer season. The former effects strengthen monsoon flows toward the continent, while the latter intensify the rainband over the ocean. Therefore, the seasonal variation of their relative importance is also responsible for the seasonality of the precipitation changes. These results suggest that competition between the opposing forces, which strengthen the land monsoon and oceanic monsoon, respectively, makes the signal of the Meiyu–Baiu rainband response smaller in July than in June; consequently there tends to be a larger spread among simulations regarding the future tendency of the rainband in July. Finally, we note that our approach of using a high-resolution AGCM has a lot of merit for studying regional climate change, as described in the Introduction, but a lack of air–sea interaction may affect the regional details of future changes, and thus more research is needed for more precise and quantitative discussions.

Supplement

Supplement 1 contains five figures (Figs. S1–S5).

Acknowledgements

The authors would like to thank Dr. M. Sugi and Dr. M. Ishii of MRI for useful comments on this study. The authors also acknowledge the anonymous reviewers for their constructive comments. This work was supported by Theme–C of the Integrated Research Program for Advancing Climate Models (TOUGOU) Grant Number JPMXD0717935561 of the Ministry of Education, Culture, Sports, Science, and Technology (MEXT) of Japan, and the

Environment Research and Technology Development Fund (JPMEERF20192004) of the Environmental Restoration and Conservation Agency of Japan.

References

Allan, R. P., and coauthors, 2020: Advances in understanding large-scale responses of the water cycle to climate change. *Annals of the New York Academy of Sciences*, **1472**, 49–75.

Bony, S., G. Bellon, D. Klocke, S. Sherwood, S. Fermepin, and S. Denvil, 2013: Robust direct effect of carbon dioxide on tropical circulation and regional precipitation. *Nat. Geosci.*, **6**, 447–451.

Chadwick, R., I. Boutle, and G. Martin, 2013: Spatial patterns of precipitation change in CMIP5: Why the rich do not get richer in the tropics. *J. Climate*, **26**, 3803–3822.

Chadwick, R., 2016: Which aspects of CO_2 forcing and SST warming cause most uncertainty in projections of tropical rainfall change over land and ocean? *J. Climate*, **29**, 2493−2509.

Chadwick, R., H. Douville, and C. B. Skinner, 2017: Timeslice experiments for understanding regional climate projections: Applications to the tropical hydrological cycle and European winter circulation. *Climate Dyn*., **49**, 3011–3029.

Chadwick, R., D. Ackerley, T. Ogura, and D. Dommenget, 2019: Separating the influences of land warming, the direct CO_2 effect, the plant physiological effect, and SST warming on regional precipitation changes. *J. Geophys. Res. Atmos*., **124**, 624–640.

Chen, C., and G. Wang, 2015: Role of North Pacific mixed layer in the response of SST annual cycle to global warming. *J. Climate*, **28**, 9451–9458.

Chen, C.-A., H.-H. Hsu, C.-C. Hong, P.-G. Chiu, C.-Y. Tu, S.-J. Lin, and A. Kitoh, 2019: Seasonal precipitation change in the western North Pacific and East Asia under global warming in two high-resolution AGCMs. *Climate Dyn*., **53**, 5583–5605.

Chen, J., and S. Bordoni, 2016: Early summer response of the East Asian summer monsoon to atmospheric CO_2 forcing and subsequent sea surface warming. *J. Climate*, **29**, 5431−5446.

Ding, Y., 2004: Seasonal march of the East-Asian summer monsoon. East Asian Monsoons. C.-P. Chang (ed.), World Scientific, Singapore, 3–53.

Endo, H., and A. Kitoh, 2014: Thermodynamic and dynamic effects on regional monsoon rainfall changes in a warmer climate, *Geophys. Res. Lett*., **41**, 1704–1710.

Endo, H., A. Kitoh, T. Ose, R. Mizuta, and S. Kusunoki, 2012: Future changes and uncertainties in Asian precipitation simulated by multi-physics and multi-sea surface temperature ensemble experiments with high-resolution Meteorological Research Institute atmospheric general circulation models (MRI-AGCMs). *J. Geophys. Res. Atmos.*, **117**, D16118, doi:10.1029/2012JD017874.

Endo, H., A. Kitoh, R. Mizuta, and M. Ishii, 2017: Future changes in precipitation extremes in East Asia and their uncertainty based on large ensemble simulations with a high-resolution AGCM. *SOLA*, **13**, 7−12.

Endo, H., A. Kitoh, and H. Ueda, 2018: A unique feature of the Asian summer monsoon response to global warming: The role of different land-sea thermal contrast change between the lower and upper troposphere. *SOLA*, **14**, 57−63.

Ha, K.-J., S. Moon, A. Timmermann, and D. Kim, 2020: Future changes of summer monsoon characteristics and evaporative demand over Asia in CMIP6 simulations. *Geophys. Res. Lett.*, **47**, e2020GL087492.

Harvey, B. J., L. C. Shaffrey, and T. J. Woollings, 2014: Equator-to-pole temperature differences and the extra-tropical storm track responses of the CMIP5 climate models. *Climate Dyn.*, **43**, 1171–1182.

He, J., and B. Soden, 2015: Anthropogenic weakening of the tropical circulation: The relative roles of direct CO_2 forcing and sea surface temperature change. *J. Climate*, **28**, 8728–8742.

He, C., B. Wu, L. Zou, and T. Zhou, 2017: Responses of the summertime subtropical anticyclones to global warming. *J. Climate*, **30**, 6465–6479.

He, C., Z. Wang, T. Zhou, and T. Li, 2019: Enhanced latent heating over the Tibetan Plateau as a key to the enhanced East Asian summer monsoon circulation under a warming climate. *J. Climate*, **32**, 3373–3388.

Held, I. M., and B. J. Soden, 2006: Robust responses of the hydrological cycle to global warming. *J. Climate*, **19**, 5686–5699.

Hirahara, S., H. Ohno, Y. Oikawa, and S. Maeda, 2012: Strengthening of the southern side of the jet stream and delayed withdrawal of Baiu season in future climate. *J. Meteor. Soc. Japan*, **90**, 663–671.

Horinouchi, T., and A. Hayashi, 2017: Meandering subtropical jet and precipitation over summertime East Asia and the northwestern Pacific. *J. Atmos. Sci*., **74**, 1233–1247.

Horinouchi, T., S. Matsumura, T. Ose, and Y. N. Takayabu, 2019: Jet-precipitation relation and future change of the Mei-Yu–Baiu rainband and subtropical jet in CMIP5 coupled GCM simulations. *J. Climate*, **32**, 2247–2259.

Huffman, G. J., R. F. Adler, D. T. Bolvin, G. Gu, E. J. Nelkin, K. P. Bowman, Y. Hong, E. F. Stocker, and D. B. Wolff, 2007: The TRMM multi-satellite precipitation analysis: Quasi-global, multi-year, combined-sensor precipitation estimates at finer scale. *J. Hydrometeor*., **8**, 38–55.

Inoue, T., and H. Ueda, 2012: Delay of the Baiu withdrawal in Japan under global warming condition with relevance to warming patterns of SST. *J. Meteor. Soc. Japan*, **90**, 855–868.

IPCC, 2013: *Climate change 2013: The physical science basis. Contribution of Working Group I to the fifth assessment report of the Intergovernmental Panel on Climate Change*. Stocker, T. F., D. Qin, G.-K. Plattner, M. Tignor, S. K. Allen, J. Boschung, A. Nauels, Y. Xia, V. Bex, and P. M. Midgley (eds.), Cambridge University Press, Cambridge, United Kingdom and New York, USA, 1535 pp.

Ito, R., T. Ose, H. Endo, R. Mizuta, K. Yoshida, A. Kitoh and T. Nakaegawa, 2020: Seasonal characteristics of future climate change over Japan and the associated atmospheric circulation anomalies in global model experiments. *Hydrol. Res. Lett.*, **14**, 130–135.

Jin, C., B. Wang, and J. Liu, 2020: Future changes and controlling factors of the eight regional monsoons projected by CMIP6 models. *J. Climate*, **33**, 9307–9326.

Kain, J. S., and J. M. Fritsch, 1990: A one-dimensional entraining/detraining plume model and its application in convective parameterization. *J. Atmos. Sci.*, **47**, 2784–2802.

Kamae, Y., M. Watanabe, M. Kimoto, and H. Shiogama, 2014: Summertime land-sea thermal contrast and atmospheric circulation over East Asia in a warming climate—part II: Importance of CO_2-induced continental warming. *Climate Dyn.*, **43**, 2569–2583.

Kimoto, M., 2005: Simulated change of the east Asian circulation under global warming scenario. *Geophys. Res. Lett.*, **32**, L16701, doi:10.1029/2005GL023383.

Kitoh, A., 2017: The Asian monsoon and its future change in climate models: A review. *J. Meteor. Soc. Japan*, **95**, 7–33.

Kitoh, A., and T. Uchiyama, 2006: Changes in onset and withdrawal of the East Asian summer rainy season by multi-model global warming experiments. *J. Meteor. Soc. Japan*, **84**, 247–258.

Kitoh, A., and S. Kusunoki, 2008: East Asian summer monsoon simulation by a 20-km mesh AGCM. *Climate Dyn.*, **31**, 389–401.

Kitoh, A., H. Endo, K. Krishna Kumar, I. F. A. Cavalcanti, P. Goswami, and T. Zhou, 2013: Monsoons in a changing world: A regional perspective in a global context. *J. Geophys. Res. Atmos.*, **118**, 3053–3065.

Kitoh, A., T. Ose, and I. Takayabu, 2016: Dynamical downscaling for climate projection with high-resolution MRI AGCM-RCM. *J. Meteor. Soc. Japan*, **94A**, 1–16.

Kobayashi, S., and coauthors, 2015: The JRA-55 reanalysis: general specifications and basic characteristics. *J. Meteor. Soc. Japan*, **93**, 5–48.

Kodama, Y.-M., 1993: Large-scale common features of subtropical convergence zones (the Baiu frontal zone, the SPCZ, and the SACZ). Part II: Conditions of the circulations for generating the STCZs. *J. Meteor. Soc. Japan*, **71**, 581–610.

Kusunoki, S., 2017: Future changes in global precipitation projected by the atmospheric model MRI-AGCM3.2H with a 60-km Size. *Atmosphere*, **8**, 93, doi:10.3390/atmos8050093.

Kusunoki, S., 2018a: Is the global atmospheric model MRI-AGCM3.2 better than the CMIP5 atmospheric models in simulating precipitation over East Asia? *Climate Dyn*., **51**, 4489–4510.

Kusunoki, S., 2018b: Future changes in precipitation over East Asia projected by the global atmospheric model MRI-AGCM3.2. *Climate Dyn*., **51**, 4601–4617.

Kusunoki, S., J. Yoshimura, H. Yoshimura, A. Noda, K. Oouchi, and R. Mizuta, 2006: Change of Baiu rain band in global warming projection by an atmospheric general circulation model with a 20-km grid size. *J. Meteor. Soc. Japan*, **84**, 581–611.

Kusunoki, S., R. Mizuta, and M. Matsueda, 2011: Future changes in the East Asian rain band projected by global atmospheric models with 20-km and 60-km grid size. *Climate*

Dyn., **37**, 2481-2493.

Li, H., A. Dai, T. Zhou, and J. Lu, 2010: Responses of East Asian summer monsoon to historical SST and atmospheric forcing during 1950–2000. *Climate Dyn*., **34**, 501–514.

Li, X., and M. Ting, 2017: Understanding the Asian summer monsoon response to greenhouse warming: the relative roles of direct radiative forcing and sea surface temperature change. *Climate Dyn*., **49**, 2863–2880.

Matsumura, S., T. Horinouchi, S. Sugimoto, and T. Sato, 2016: Response of the Baiu rainband to northwest Pacific SST anomalies and its impact on atmospheric circulation. *J. Climate*, **29**, 3075–3093.

Matsumura, S., S. Ueki, and T. Horinouchi, 2019: Contrasting responses of midlatitude jets to the North Pacific and North Atlantic warming. *Geophys. Res. Lett*., **46**, 3973–3981.

Mizuta, R., Y. Adachi, S. Yukimoto, and S. Kusunoki, 2008: Estimation of future distribution of sea surface temperature and sea ice using CMIP3 multi-model ensemble mean. *Techical Reports of the MRI*, **56**, 28 pp., doi:10.11483/mritechrepo.56.

Mizuta, R., H. Yoshimura, H. Murakami, M. Matsueda, H. Endo, T. Ose, K. Kamiguchi, M. Hosaka, M. Sugi, S. Yukimoto, S. Kusunoki, and A. Kitoh, 2012: Climate simulations using MRI-AGCM3.2 with 20-km grid. *J. Meteor. Soc. Japan*, **90A**, 233–258.

Mizuta, R., O. Arakawa, T. Ose, S. Kusunoki, H. Endo, and A. Kitoh, 2014: Classification of CMIP5 future climate responses by the tropical sea surface temperature changes. *SOLA*, **10**, 167−171.

Mizuta, R., and coauthors, 2017: Over 5000 years of ensemble future climate simulations by 60km global and 20km regional atmospheric models. *Bull. Am. Meteor. Soc.*, **98**, 1383–1398.

Nakamura, M., and T. Miyama, 2014: Impacts of the Oyashio temperature front on the regional climate. *J. Climate*, **27**, 7861–7873.

Ninomiya, K., 2004: Large- and mesoscale features of Meiyu-Baiu front associated with intense rainfalls. *East Asian Monsoons*, C.-P. Chang (ed.), World Scientific, Singapore, 404–435.

Nishii, K., B. Taguchi, and H. Nakamura, 2020: An atmospheric general circulation model assessment of oceanic impacts on extreme climatic events over Japan in July 2018. *J. Meteor. Soc. Japan*, **98**, 801–820.

Ogata, T., H. Ueda, T. Inoue, M. Hayasaki, A. Yoshida, S. Watanabe, M. Kira, M. Ooshiro, and A. Kumai, 2014: Projected future changes in the Asian monsoon: A comparison of CMIP3 and CMIP5 model results. *J. Meteor. Soc. Japan*, **92**, 207–225.

Ose, T., 2019a: Characteristics of future changes in summertime East Asian monthly precipitation in MRI-AGCM global warming experiments. *J. Meteor. Soc. Japan*, **97**, 317–335.

Ose, T., 2019b: Future changes in summertime East Asian monthly precipitation in CMIP5 and their dependence on present-day model climatology. *J. Meteor. Soc. Japan*, **97**, 1041–1053.

Ose, T., Y. Takaya, S. Maeda, and T. Nakaegawa, 2020: Resolution of summertime East Asian pressure pattern and southerly monsoon wind in CMIP5 multi-model future projections. *J. Meteor. Soc. Japan*, **98**, 927–944.

Qu, X., and G. Huang, 2020: CO_2-induced heat source changes over the Tibetan Plateau in boreal summer-part II: the effects of CO_2 direct radiation and uniform sea surface warming. *Climate Dyn*., **55**, 1631–1647.

Randall, D. A., and D.-M. Pan, 1993: Implementation of the Arakawa-Schubert cumulus parameterization with a prognostic closure. *The representation of cumulus convection in numerical models*. K. A. Emanuel and D. J. Raymond (eds.), American Meteorological Society, USA, *Meteorol. Monogr*., **24**, (46), 137–144.

Rayner, N. A., D. E. Parker, E. B. Horton, C. K. Folland, L. V. Alexander, D. P. Rowell, E. C. Kent, and A. Kaplan, 2003: Global analyses of sea surface temperature, sea ice, and night marine air temperature since the late nineteenth century. *J. Geophys. Res*., **108**, 4407, doi:10.1029/2002JD002670.

Sampe, T., and S.-P. Xie, 2010: Large-scale dynamics of the Meiyu-Baiu rainband: Environmental forcing by the westerly jet. *J. Climate*, **23**, 113–134.

Santer, B. D., S. Po-Chedley, M. D. Zelinka, I. Cvijanovic, C. Bonfils, P. J. Durack, Q. Fu, J. Kiehl, C. Mears, J. Painter, G. Pallotta, S. Solomon, F. J. Wentz, and C.-Z. Zou, 2018: Human influence on the seasonal cycle of tropospheric temperature. *Science* **361**, eaas8806, doi:10.1126/science.aas8806.

Shaw, T. A., and A. Voigt, 2015: Tug of war on summertime circulation between radiative forcing and sea surface warming. *Nat. Geosci*., **8**, 560–566.

Song, F., T. Zhou, and Y. Qian, 2014: Responses of East Asian summer monsoon to natural and anthropogenic forcings in the 17 latest CMIP5 models. *Geophys. Res. Lett*., **41**, 596–603.

Suzuki, S.-I., and B. Hoskins, 2009: The large-scale circulation change at the end of the Baiu season in Japan as seen in ERA40 data. *J. Meteor. Soc. Japan*, **87**, 83–99.

Tokioka, T., and M. Saito, 1992: Numerical experiments on the characteristics of ocean/continent-scale climate changes in global warming produced by CO_2 increase. *Proceedings of the Workshop on the Effects of Global Climate Change on Hydrology and Water Resources at the Catchment Scale*, 3–6 February 1992, Tsukuba, Japan, 57–66.

Wang, B., and LinHo, 2002: Rainy season of the Asian-Pacific summer monsoon. *J. Climate*, **15**, 386–398.

Wang, B., Q. Ding, X. Fu, I.-S. Kang, K. Jin, J. Shukla, and F. Doblas-Reyes, 2005: Fundamental challenge in simulation and prediction of summer monsoon rainfall. *Geophys. Res. Lett*., **32**, L15711, doi:10.1029/2005GL022734.

Wang, B., Z. Wu, J. Li, J. Liu, C. Chang, Y. Ding, and G. Wu, 2008: How to measure the strength of the East Asian summer monsoon. *J. Climate*, **21**, 4449–4463.

Wang, B., and coauthors, 2020: Monsoons climate change assessment. *Bull. Amer. Meteor. Soc*., doi: https://doi.org/10.1175/BAMS-D-19-0335.1.

Xie, S.-P., C. Deser, G. A. Vecchi, J. Ma, H. Teng and A. T. Wittenberg, 2010: Global warming pattern formation: sea surface temperature and rainfall. *J. Climate*, **23**, 966–986.

Yamaguchi, M., J. C. L. Chan, I.-J. Moon, K. Yoshida, and R. Mizuta, 2020: Global warming changes tropical cyclone translation speed. *Nat. Commun.,* **11**, 47, doi:10.1038/s41467-019-13902-y.

Yoshimura, H., R. Mizuta, and H. Murakami, 2015: A spectral cumulus parameterization scheme interpolating between two convective updrafts with semi-Lagrangian calculation of transport by compensatory subsidence. *Mon. Wea. Rev.*, **143**, 597–621.

Zhou, S., G. Huang, and P. Huang, 2018: Changes in the East Asian summer monsoon rainfall under global warming: Moisture budget decomposition and the sources of uncertainty. *Climate Dyn*., **51**, 1363–1373.

Zhou, T., and L. Zou, 2010: Understanding the predictability of East Asian summer monsoon from the reproduction of land–sea thermal contrast change in AMIP-type simulation. *J. Climate*, **23**, 6009–6026.

List of Figures

Fig. 1. Present-day climate simulation showing precipitation (shading, mm day^{-1}), sea-level pressure (black contour; 4 hPa interval), and 300-hPa zonal wind (purple thick contour; 5 m s^{-1} interval for winds over 15 m s^{-1}) from (a–d) observations and reanalysis, (e–h) the MRI-AGCM60 with the YS cumulus scheme, (i–l) the MRI-AGCM60 ensemble mean with

the YS/AS/KF cumulus schemes, and (m–p) the CMIP5 AOGCM ensemble mean. (a, e, i, m) June–August mean, (b, f, j, n) June, (c, g, k, o) July, and (d, h, l, p) August. In (a–d), TRMM-3B42 (Huffman et al. 2007) and JRA-55 (Kobayashi et al. 2015) are used as precipitation data and atmospheric circulation data, respectively. Sea-level pressure and 300-hPa zonal wind data are re-gridded onto a 2.5° longitude by 2.5° latitude mesh. Sea level pressure data with an altitude exceeding 1500 m are not drawn. The period analyzed is 1998–2015 for (a–d), 1979–2003 for (e–h) and (m–p), and 1984–2003 for (i–l).

Fig. 2. Precipitation changes (mm day^{-1}) between the present and the end of the 21st century under the RCP8.5 scenario from (a–d) multi-SST ensemble projections with MRI-AGCM60 (28 members), (e–h) multi-physics and multi-SST ensemble projections with MRI-AGCM60 (12 members), and (i–l) CMIP5 AOGCM ensemble projections (28 models). (a, e, i) June–August mean, (b, f, j) June, (c, g, k) July, and (d, h, l) August. Thick contours indicate 7 mm day^{-1} isolines for the present day based on data re-gridded onto a 2.5° longitude by 2.5° latitude mesh. The period of the present-day (future) climate simulation is 1979–2003 (2075–2099) for (a–d) and (i–l), and 1984–2003 (2080–2099) for (e–h). Hatching represents areas where changes have the same sign in more than 80% of the simulations.

Fig. 3. As in Fig. 2, except for sea-level pressure (shading; hPa), 850-hPa wind anomalies

(vector; m s^{-1}), and 300-hPa zonal wind (contour; m s^{-1}). For sea-level pressure, the areas where changes have the same sign in more than 80% of the simulations are shown by hatching. For 300-hPa zonal wind, 15 m s^{-1} isolines are drawn in magenta (white) for the present (future) simulation. Sea-level pressure and 300-hPa zonal wind data are drawn based on data re-gridded onto a 2.5° longitude by 2.5° latitude mesh. Thick black contours represent an elevation of 1500 m.

Fig. 4. Time–latitude cross-section of future changes averaged over 125°E–145°E (shading) for (a–c) precipitation (mm day^{-1}) and (d–f) 300-hPa zonal wind (m s^{-1}). (a, d) multi-SST ensemble projections with MRI-AGCM60 (28 members), (b, e) multi-physics and multi-SST ensemble projections with MRI-AGCM60 (12 members), and (c, f) CMIP5 AOGCM ensemble projections (28 models). Black contours denote the present-day simulation. White contours in (d–f) denote the future simulation. Hatching shows areas where changes have the same sign in more than 80% of the simulations. All the panels are drawn based on monthly output re-gridded onto a 2.5° longitude by 2.5° latitude mesh.

Fig. 5. Sensitivity experiments with the MRI-AGCM60 in June for (a–e) surface air temperature (SAT; K), (f–j) precipitation (mm day^{-1}), and (k–o) 200-hPa zonal wind (U200; m s^{-1}). (a, f, k) All forcing (HF minus HP; ALL), (b, g, l) direct GHG radiative forcing (Exp1 minus HP; GHGrad), (c, h, m) uniform SST warming (Exp2 minus HP; SSTunif), (d, i, n)

SST pattern change in the tropics (HF minus Exp3; SSTtp), and (e, j, o) SST pattern change in the NH extratropics (HF minus Exp4; SSTnh). Shading denotes areas where changes are statistically significant at the 95% confidence level, except for (a–e). In (k–o), contours denote the HP-run climatology with 20 m s^{-1} isolines.

Fig. 6. As in Fig. 5, but for August.

Fig. 7. Spatial correlation coefficient between the future changes with all forcing (ALL) and each effect isolated from the sensitivity experiments over the area 0°E–360°E, 20°S–80°N from June to August for (a) surface air temperature, (b) precipitation, (c) sea-level pressure, (d) 200-hPa zonal wind, and (e) 500-hPa vertical velocity. For sea-level pressure data, areas where the altitude exceeds 1500 m are excluded from the calculation.

Fig. 8. As in Fig. 7, but for East Asia (100°E–160°E, 20°N–50°N) and for (f) 850hPa meridional wind.

Fig. 9. As in Fig. 5, but for precipitation changes (mm day^{-1}) and (e–h) the sum of the four effects (i.e., GHGrad, SSTunif, SSTtp, and SSTnh). Columns from left to right show the June–August mean, June, July, and August, respectively. Hatching denotes areas where changes are statistically significant at the 95% confidence level. Thick contours indicate 7

mm day^{-1} isolines for the HP-run climatology based on data re-gridded onto 2.5° latitude/longitude grids.

Fig. 10. Sensitivity experiments with the MRI-AGCM60 showing time–latitude cross-sections of precipitation (shading; mm day^{-1}) averaged over 125°E–145°E. (a) RCP8.5 scenario (HF minus HP; ALL), (b) sum of (c)–(f), (c) GHG radiative forcing (Exp1 minus HP; GHGrad), (d) uniform SST warming (Exp2 minus HP; SSTunif), (e) SST pattern change over the NH extra-tropics (HF minus Exp4; SSTnh), (f) SST pattern change over the tropics (HF minus Exp3; SSTtp). Contours indicate the HP-run climatology. Hatching indicates that the change is statistically significant at the 95% confidence level.

Fig. 11. As in Fig. 9, but for sea-level pressure (shading; hPa), 850-hPa wind anomalies (vector; m s^{-1}), and 300-hPa zonal wind (contour; m s^{-1}). For sea-level pressure, areas where changes are statistically significant at the 95% confidence level are shown by hatching. For 300-hPa zonal wind, 15 m s^{-1} isolines are drawn in magenta for the HP-run climatology, and in white for the response of the sensitivity experiment. All are drawn based on data re-gridded onto a 2.5° longitude by 2.5° latitude mesh. Thick black contours represent an elevation of 1500 m.

Fig. 12. As in Fig. 10, but for changes in 300-hPa zonal wind (shading; m s^{-1}). Black contours

show the HP-run climatology, and white contours show the response of the sensitivity experiment.

Fig. 13. As in Fig. 10, but for changes in the thickness temperature (shading; K) averaged in the troposphere (i.e., the surface up to 300 hPa) and the HP-run climatology of 300-hPa zonal wind (contours). Note that the color scale is not the same in all panels and there is no information about the statistical significance of the changes.

Fig. 14. Time–latitude cross-section averaged over 100°E–160°E for (a) the surface air temperature anomaly in HF minus HP (ALL), (b) the land surface temperature anomaly in Exp1 minus HP (GHGrad), and (c) the sea surface temperature anomaly in HF minus Exp4 (SSTnh), shown by shading. The HP-run climatology is indicated by contours. The units are given in degrees Celsius.

List of Tables

Table 1. Experimental design for the multi-SST ensemble projections.

Table 2. Experimental design for the multi-physics and multi-SST ensemble projection.

Table 3. List of sensitivity experiments with the MRI-AGCM60.

920

Fig. 1

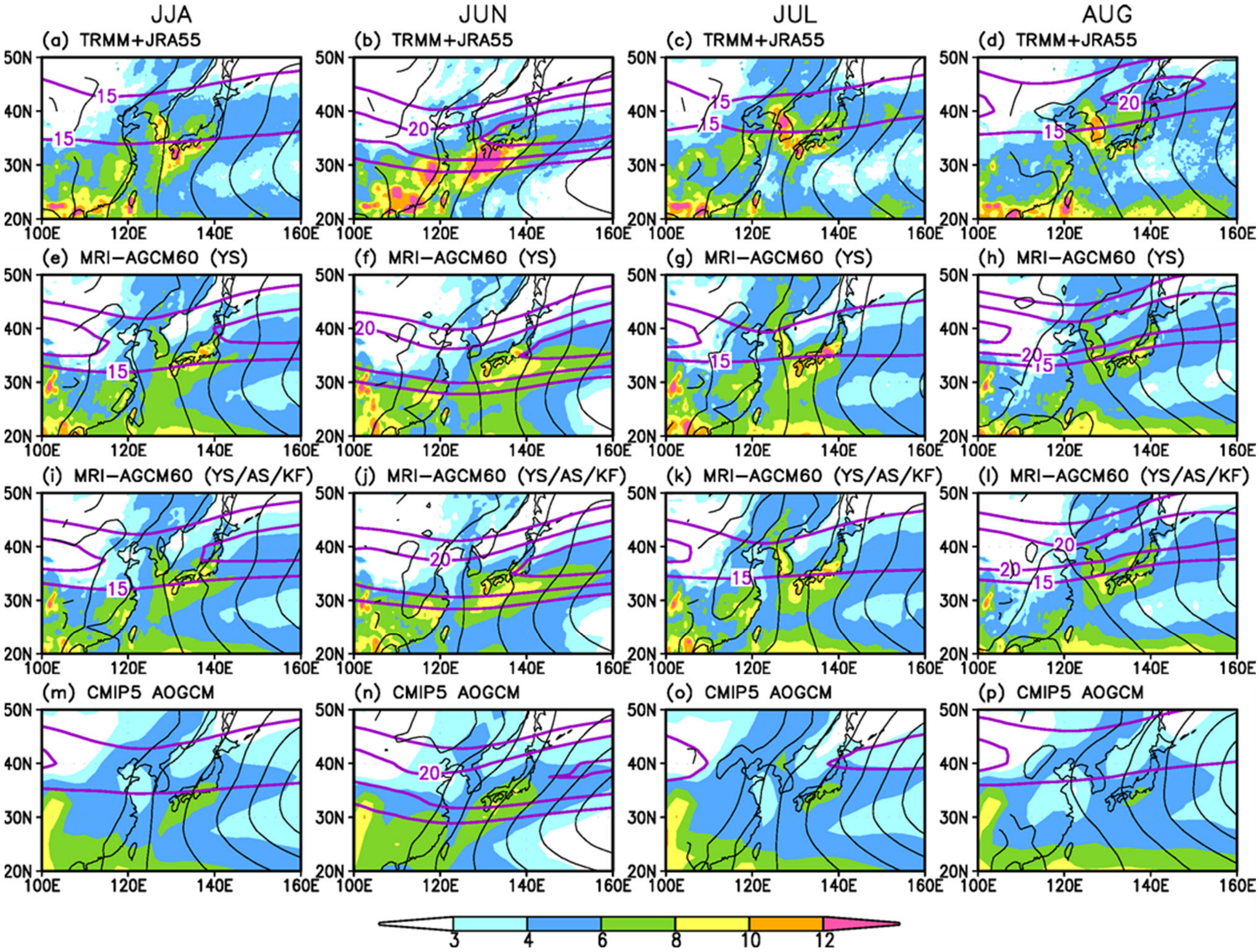
JJA
JUN
JUL
AUG
(a) TRMM+JRA55
(b) TRMM+JRA55
(c) TRMM+JRA55
(d) TRMM+JRA55
(e) MRI−AGCM60 (YS)
(f) MRI−AGCM60 (YS)
(g) MRI−AGCM60 (YS)
(h) MRI−AGCM60 (YS)
(i) MRI−AGCM60 (YS/AS/KF)
(j) MRI−AGCM60 (YS/AS/KF)
(k) MRI−AGCM60 (YS/AS/KF)
(l) MRI−AGCM60 (YS/AS/KF)
(m) CMIP5 AOGCM
(n) CMIP5 AOGCM
(o) CMIP5 AOGCM
(p) CMIP5 AOGCM
3 4 6 8 10 12

Fig. 2

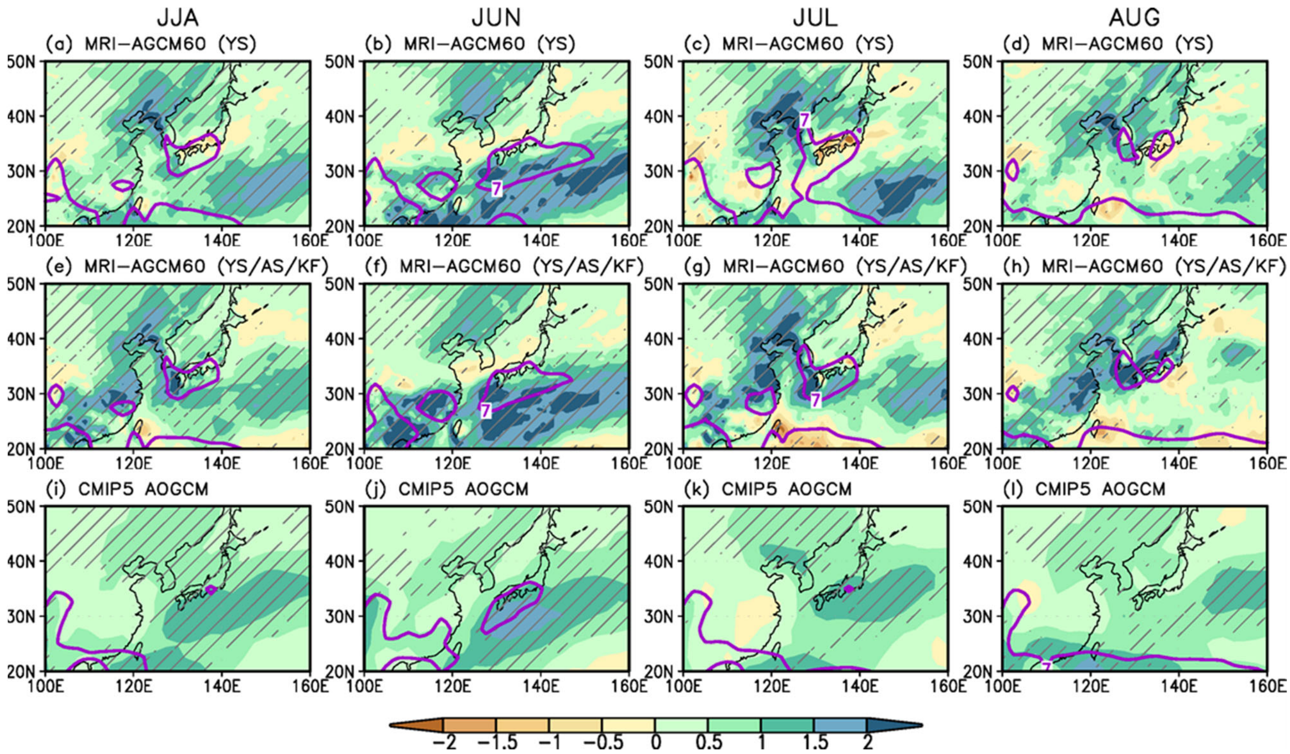

JJA
JUN
JUL
AUG
(a) MRI−AGCM60 (YS)
(b) MRI−AGCM60 (YS)
(c) MRI−AGCM60 (YS)
(d) MRI−AGCM60 (YS)
(e) MRI−AGCM60 (YS/AS/KF)
(f) MRI−AGCM60 (YS/AS/KF)
(g) MRI−AGCM60 (YS/AS/KF)
(h) MRI−AGCM60 (YS/AS/KF)
(i) CMIP5 AOGCM
(j) CMIP5 AOGCM
(k) CMIP5 AOGCM
(l) CMIP5 AOGCM
50N
40N
30N
20N
100E
120E
140E
160E
7
−2 −1.5 −1 −0.5 0 0.5 1 1.5 2

Fig. 3

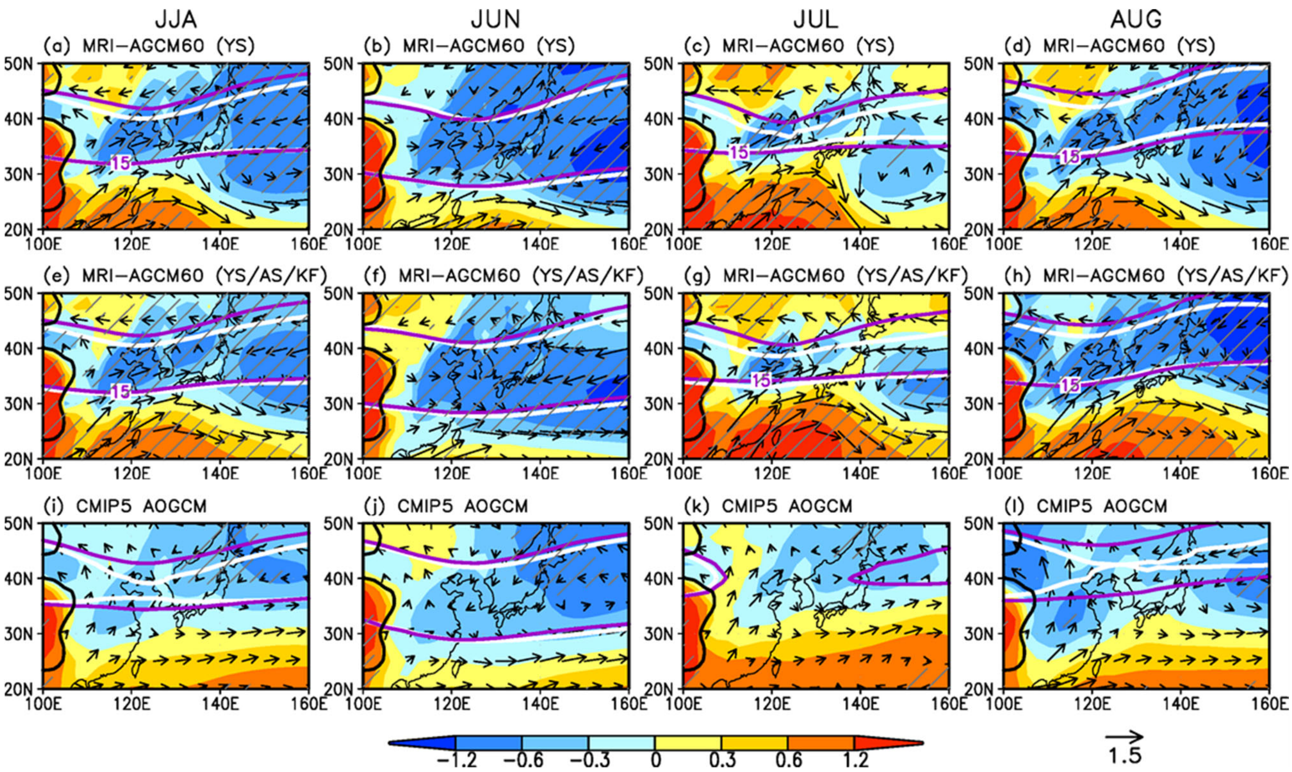
JJA
JUN
JUL
AUG
(a) MRI−AGCM60 (YS)
(b) MRI−AGCM60 (YS)
(c) MRI−AGCM60 (YS)
(d) MRI−AGCM60 (YS)
(e) MRI−AGCM60 (YS/AS/KF)
(f) MRI−AGCM60 (YS/AS/KF)
(g) MRI−AGCM60 (YS/AS/KF)
(h) MRI−AGCM60 (YS/AS/KF)
(i) CMIP5 AOGCM
(j) CMIP5 AOGCM
(k) CMIP5 AOGCM
(l) CMIP5 AOGCM
50N
40N
30N
20N
100E
120E
140E
160E
15
−1.2
−0.6
−0.3
0
0.3
0.6
1.2
1.5

Fig. 4

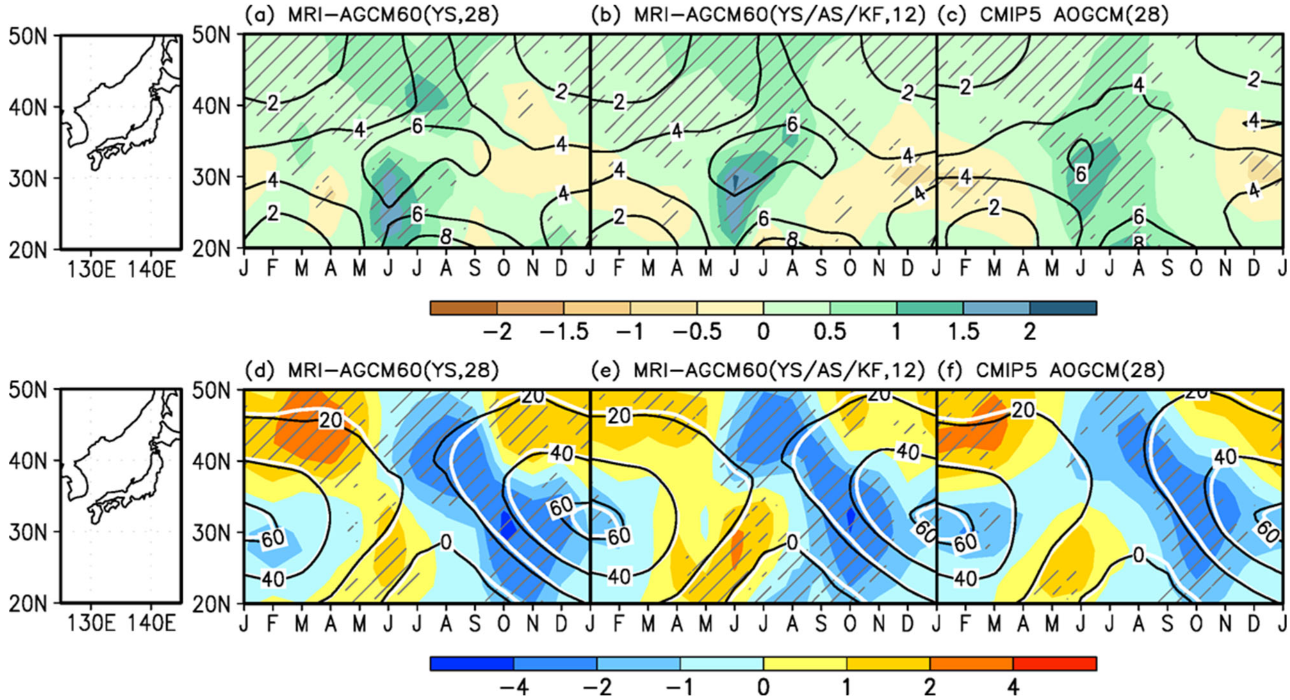
(a) MRI−AGCM60(YS,28)
(b) MRI−AGCM60(YS/AS/KF,12)
(c) CMIP5 AOGCM(28)
(d) MRI−AGCM60(YS,28)
(e) MRI−AGCM60(YS/AS/KF,12)
(f) CMIP5 AOGCM(28)
50N
40N
30N
20N
130E 140E
J F M A M J J A S O N D J
−2 −1.5 −1 −0.5 0 0.5 1 1.5 2
−4 −2 −1 0 1 2 4

Fig. 5

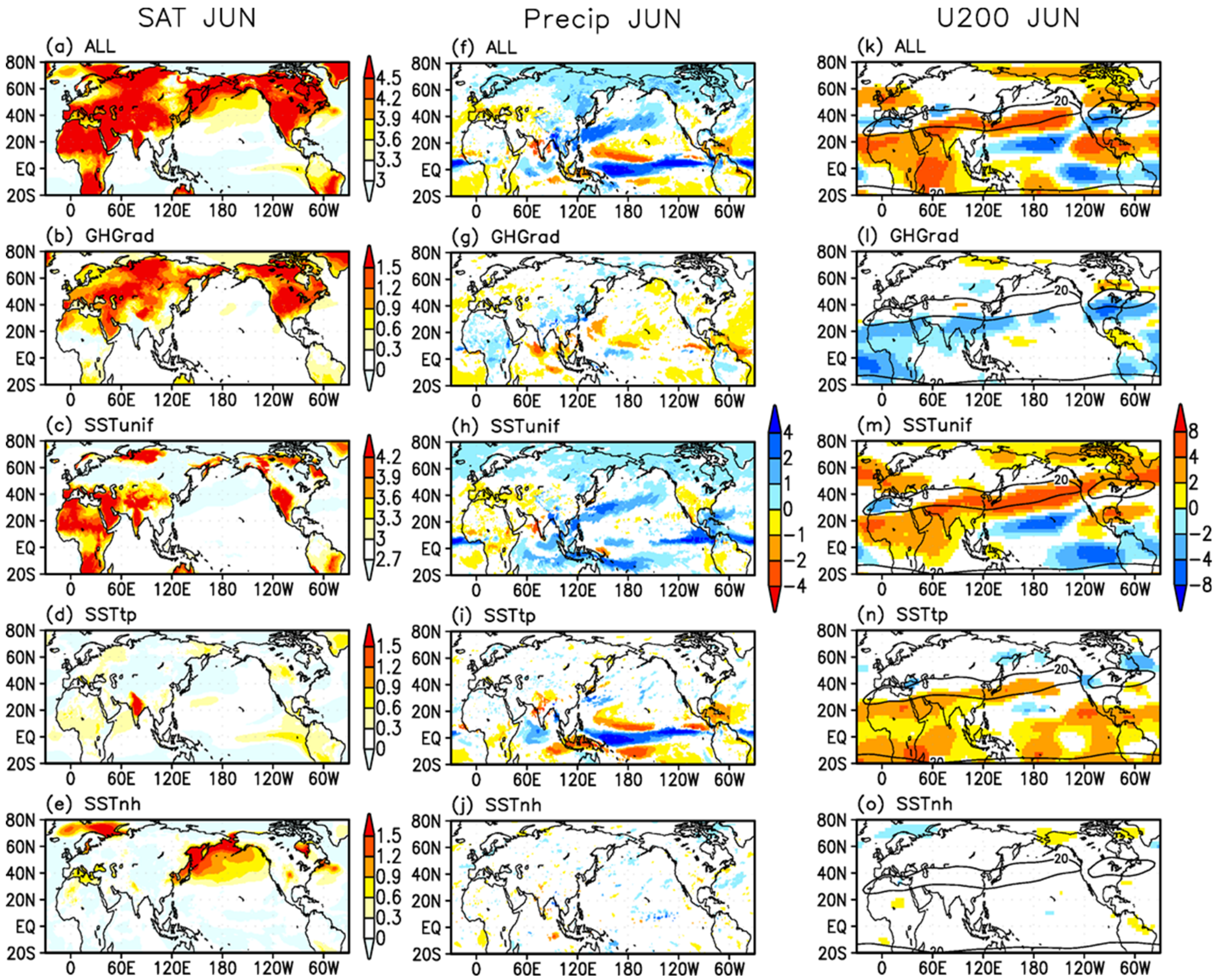
SAT JUN
Precip JUN
U200 JUN
(a) ALL
(b) GHGrad
(c) SSTunif
(d) SSTtp
(e) SSTnh
(f) ALL
(g) GHGrad
(h) SSTunif
(i) SSTtp
(j) SSTnh
(k) ALL
(l) GHGrad
(m) SSTunif
(n) SSTtp
(o) SSTnh
80N 60N 40N 20N EQ 20S
0 60E 120E 180 120W 60W
3 3.3 3.6 3.9 4.2 4.5
0 0.3 0.6 0.9 1.2 1.5
2.7 3 3.3 3.6 3.9 4.2
−4 −2 −1 0 1 2 4
−8 −4 −2 0 2 4 8
20

Fig. 6

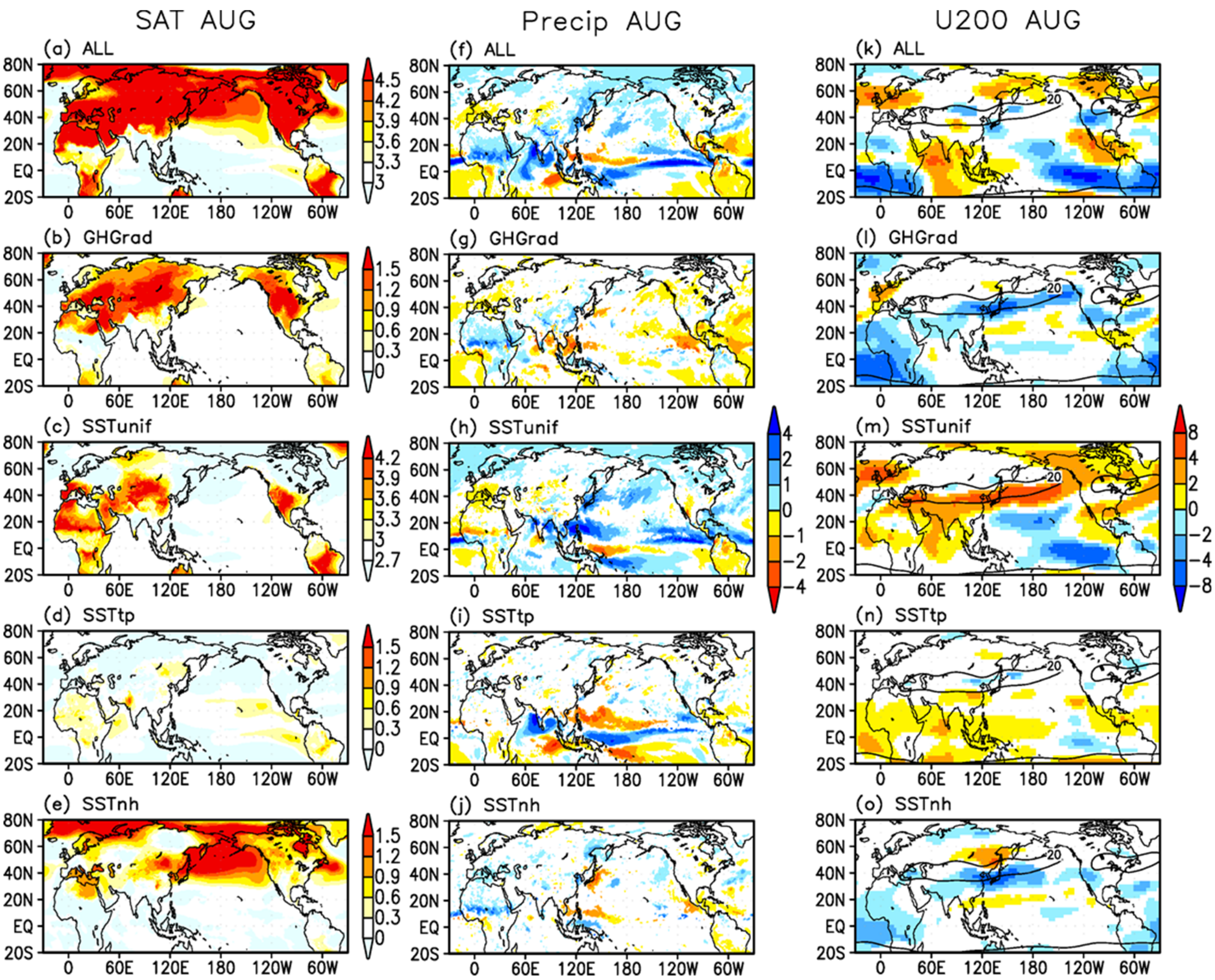
SAT AUG
Precip AUG
U200 AUG
(a) ALL
(b) GHGrad
(c) SSTunif
(d) SSTtp
(e) SSTnh
(f) ALL
(g) GHGrad
(h) SSTunif
(i) SSTtp
(j) SSTnh
(k) ALL
(l) GHGrad
(m) SSTunif
(n) SSTtp
(o) SSTnh
80N 60N 40N 20N EQ 20S
0 60E 120E 180 120W 60W
20

Fig. 7

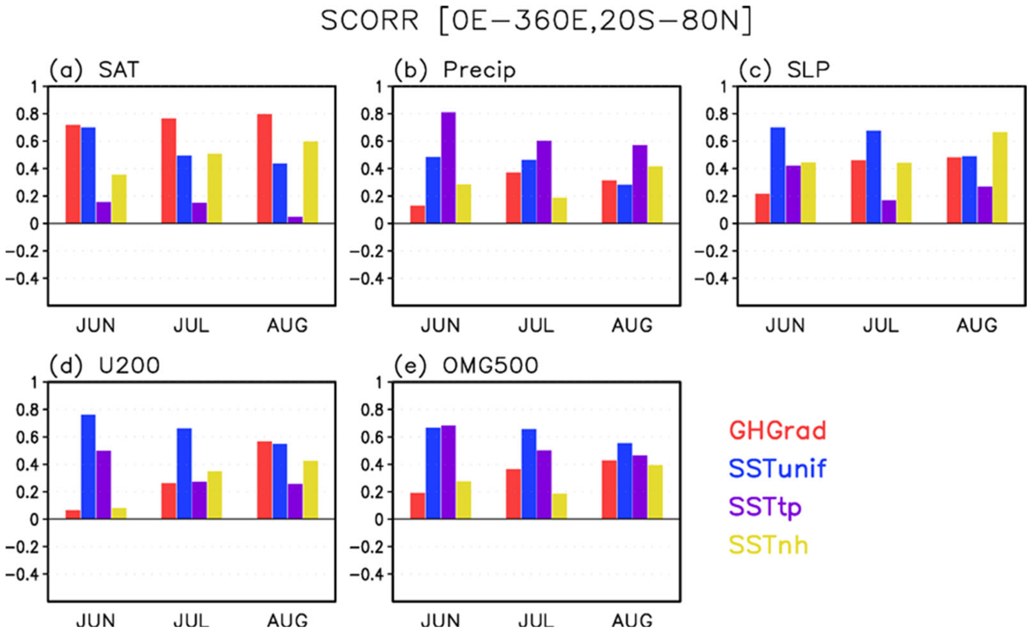
SCORR [0E–360E,20S–80N]
(a) SAT
(b) Precip
(c) SLP
(d) U200
(e) OMG500
JUN
JUL
AUG
GHGrad
SSTunif
SSTtp
SSTnh

Fig. 8

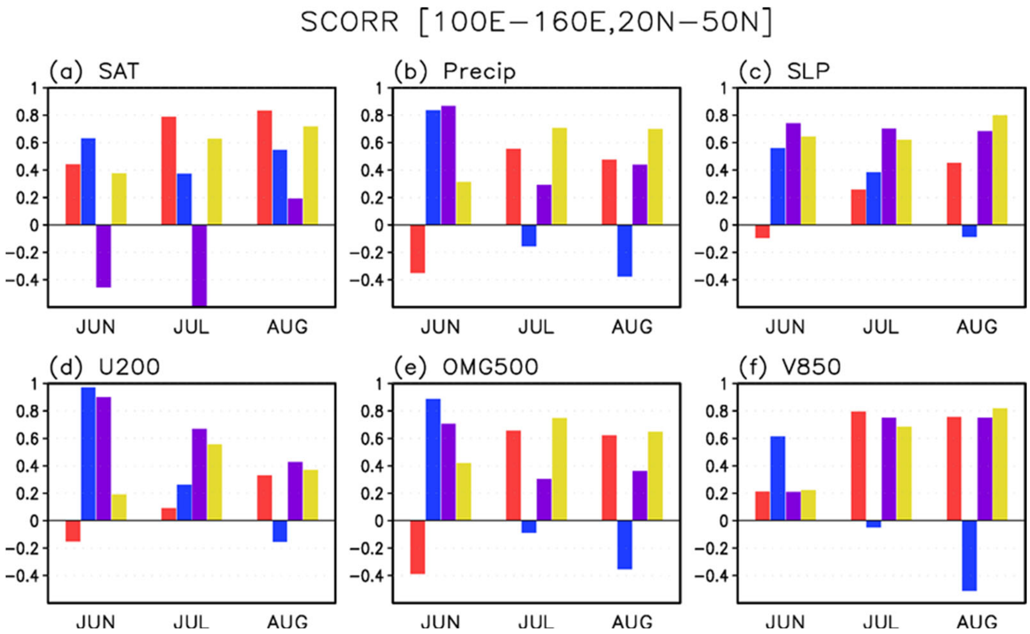
SCORR [100E–160E,20N–50N]
(a) SAT
(b) Precip
(c) SLP
(d) U200
(e) OMG500
(f) V850
JUN
JUL
AUG

Fig. 9

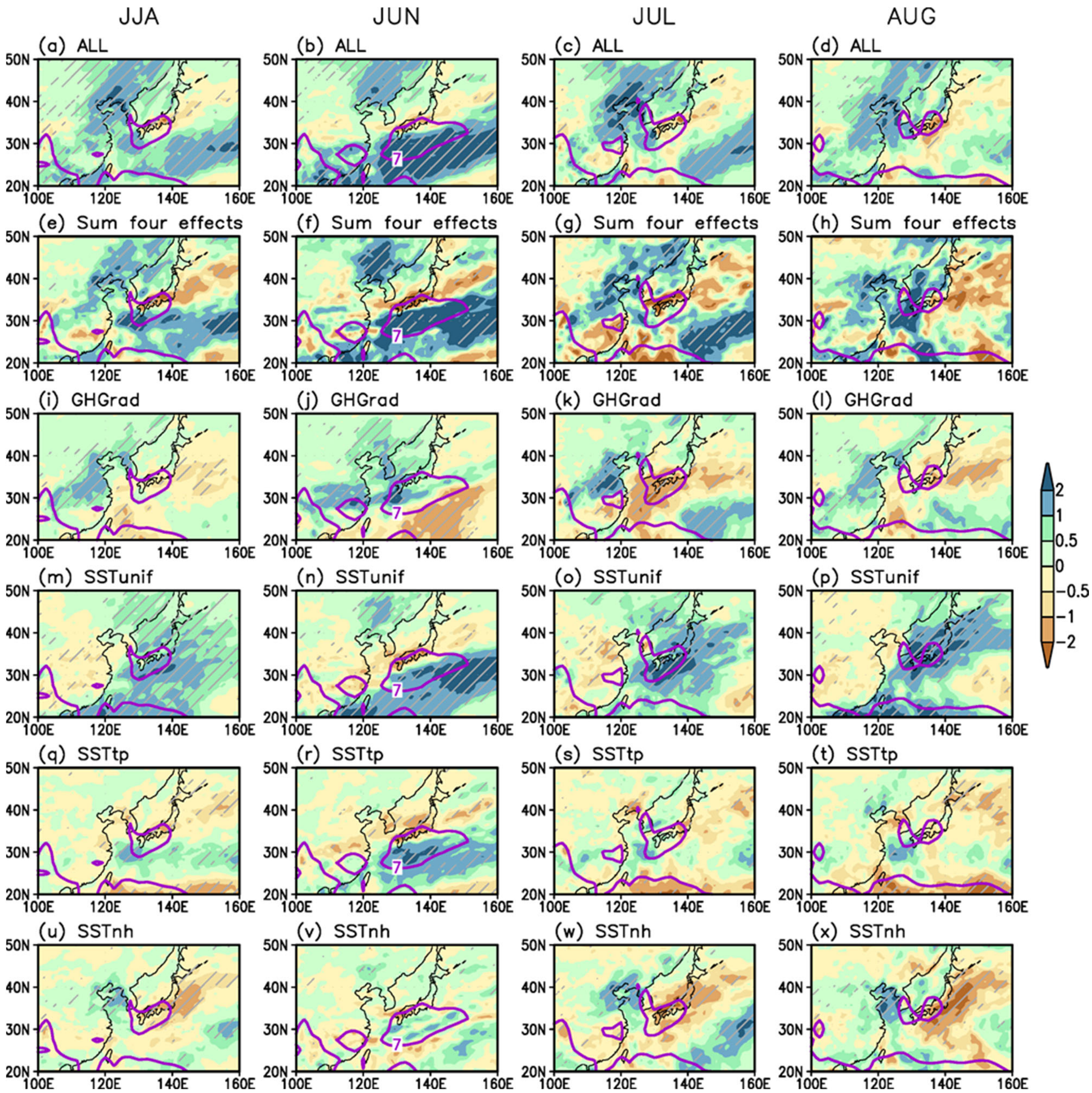

JJA
JUN
JUL
AUG
(a) ALL
(b) ALL
(c) ALL
(d) ALL
(e) Sum four effects
(f) Sum four effects
(g) Sum four effects
(h) Sum four effects
(i) GHGrad
(j) GHGrad
(k) GHGrad
(l) GHGrad
(m) SSTunif
(n) SSTunif
(o) SSTunif
(p) SSTunif
(q) SSTtp
(r) SSTtp
(s) SSTtp
(t) SSTtp
(u) SSTnh
(v) SSTnh
(w) SSTnh
(x) SSTnh
50N
40N
30N
20N
100E
120E
140E
160E
7
2
1
0.5
0
−0.5
−1
−2

Fig. 10

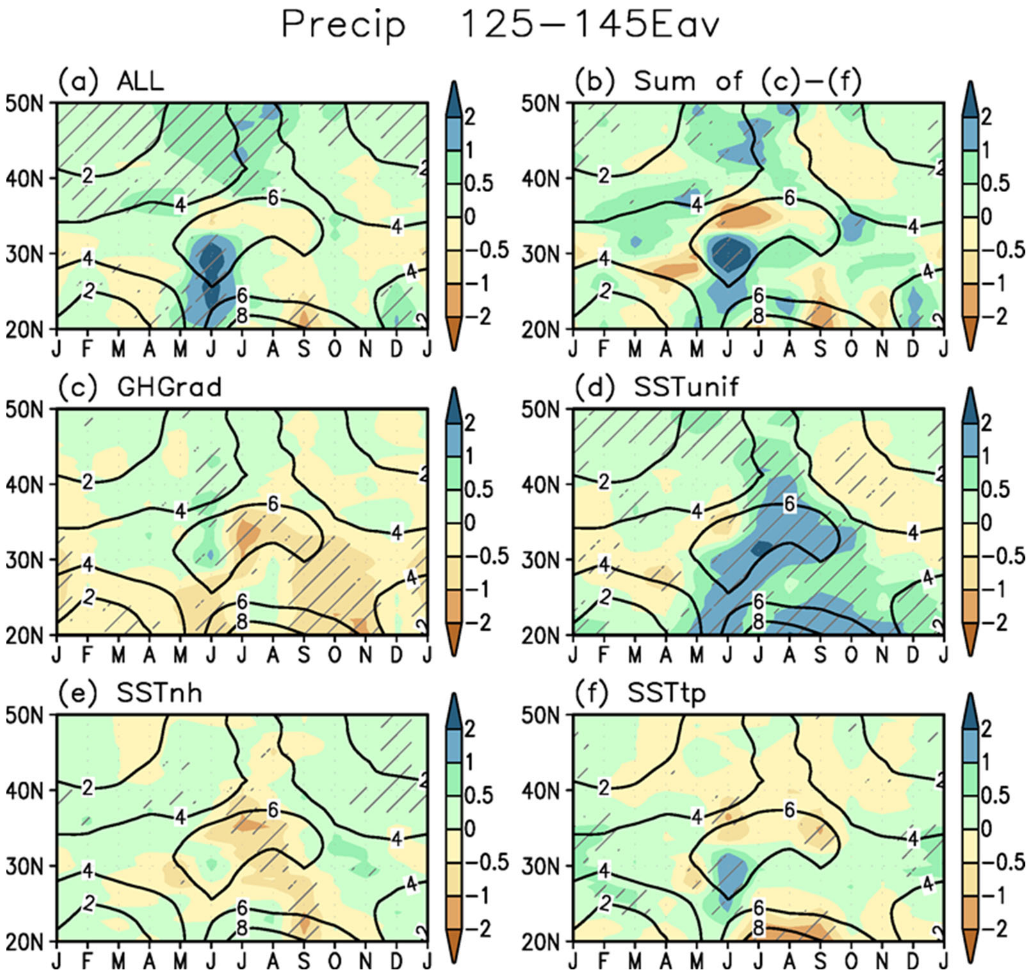

Precip 125−145Eav
(a) ALL
(b) Sum of (c)−(f)
(c) GHGrad
(d) SSTunif
(e) SSTnh
(f) SSTtp
50N
40N
30N
20N
J F M A M J J A S O N D J
2
1
0.5
0
−0.5
−1
−2

Fig. 11

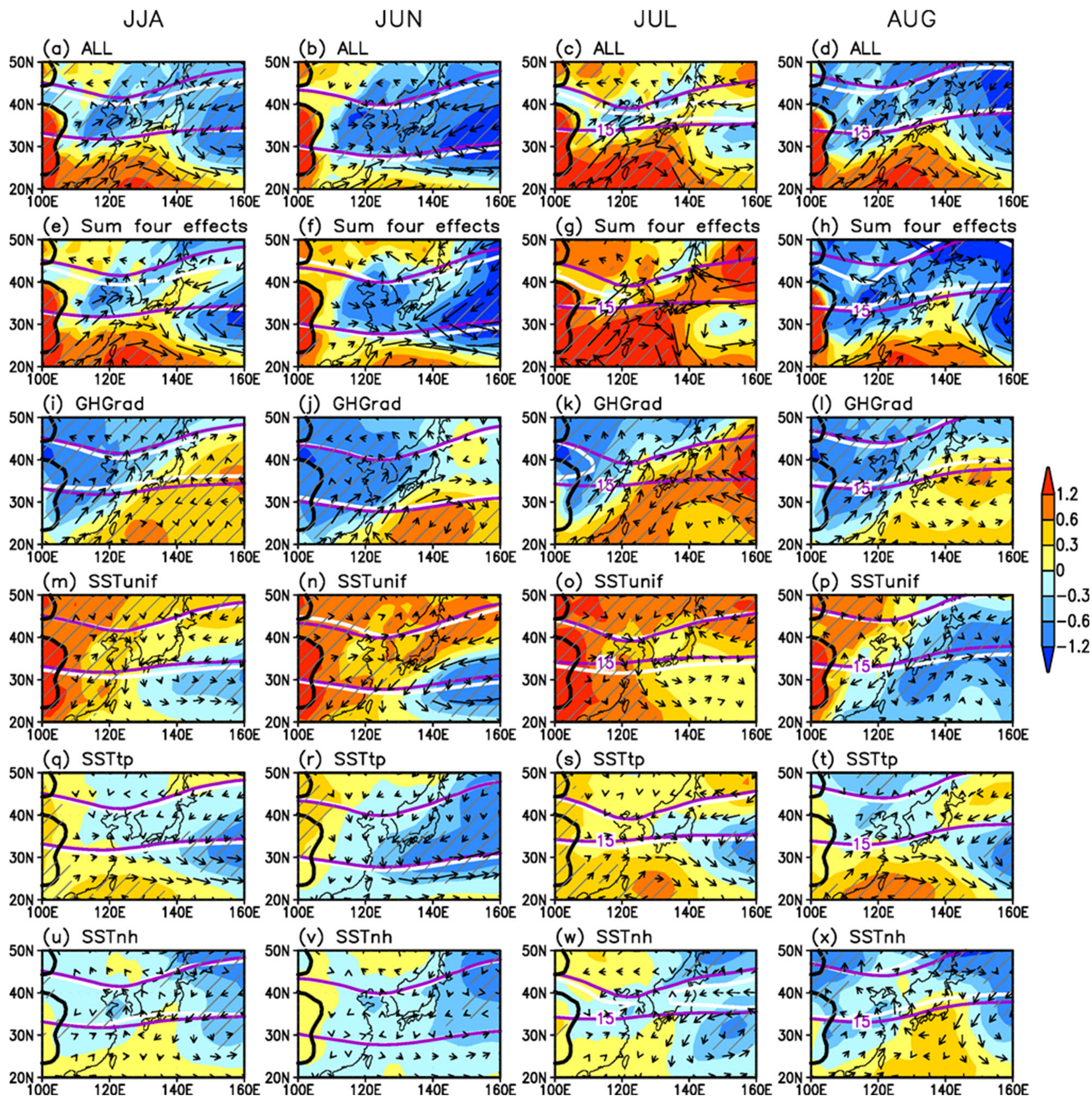
JJA
JUN
JUL
AUG
(a) ALL
(b) ALL
(c) ALL
(d) ALL
(e) Sum four effects
(f) Sum four effects
(g) Sum four effects
(h) Sum four effects
(i) GHGrad
(j) GHGrad
(k) GHGrad
(l) GHGrad
(m) SSTunif
(n) SSTunif
(o) SSTunif
(p) SSTunif
(q) SSTtp
(r) SSTtp
(s) SSTtp
(t) SSTtp
(u) SSTnh
(v) SSTnh
(w) SSTnh
(x) SSTnh
50N
40N
30N
20N
100E
120E
140E
160E
15
1.2
0.6
0.3
0
−0.3
−0.6
−1.2

Fig. 12

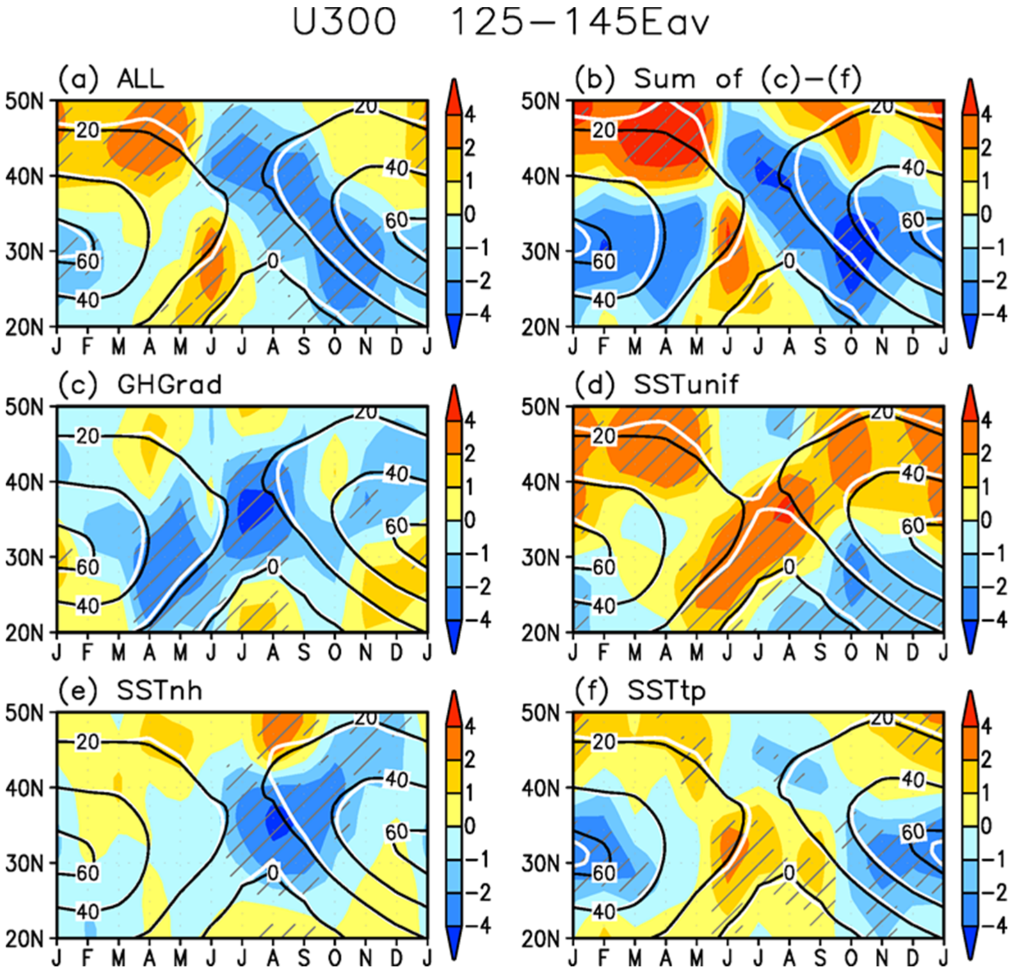

U300 125−145Eav
(a) ALL
(b) Sum of (c)−(f)
(c) GHGrad
(d) SSTunif
(e) SSTnh
(f) SSTtp
50N
40N
30N
20N
J F M A M J J A S O N D J
20
40
60
0
4
2
1
0
−1
−2
−4

Fig. 13

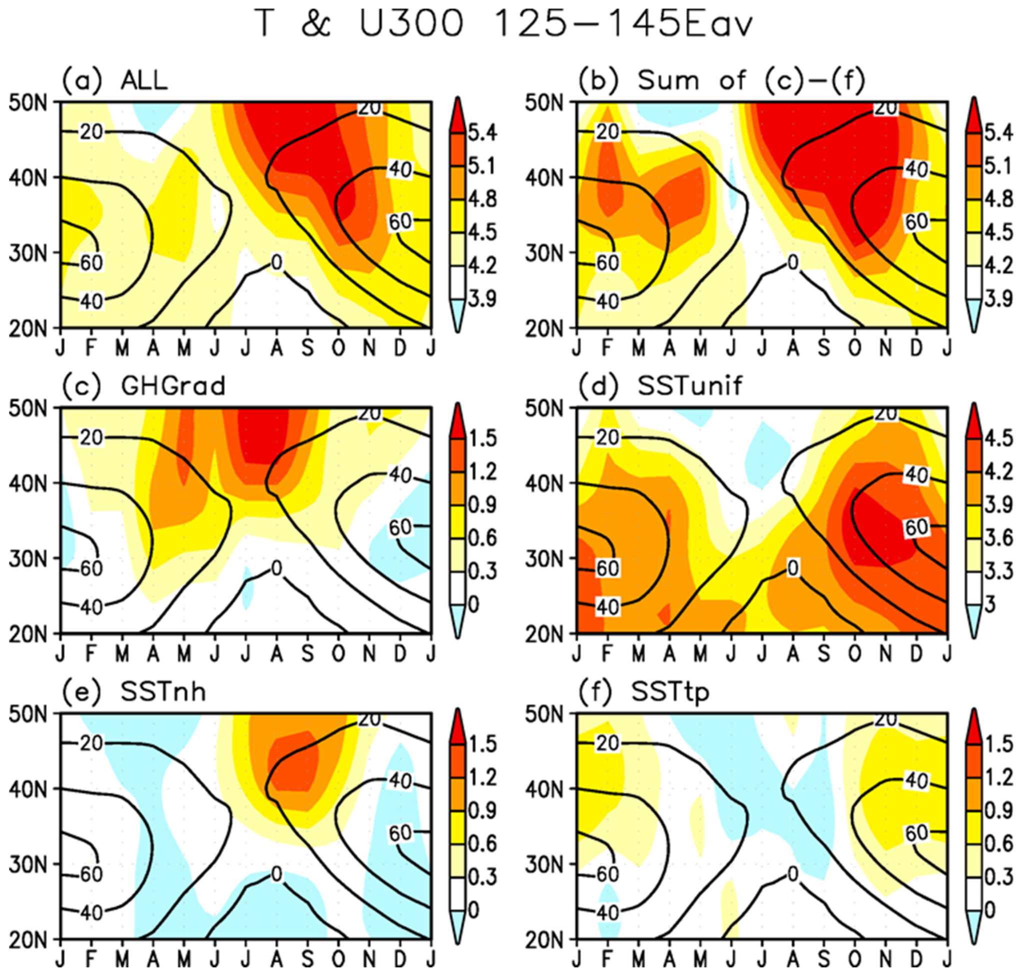
T & U300 125−145Eav
(a) ALL
(b) Sum of (c)−(f)
(c) GHGrad
(d) SSTunif
(e) SSTnh
(f) SSTtp
50N
40N
30N
20N
J F M A M J J A S O N D J
5.4
5.1
4.8
4.5
4.2
3.9
1.5
1.2
0.9
0.6
0.3
0
4.5
4.2
3.9
3.6
3.3
3

Fig. 14

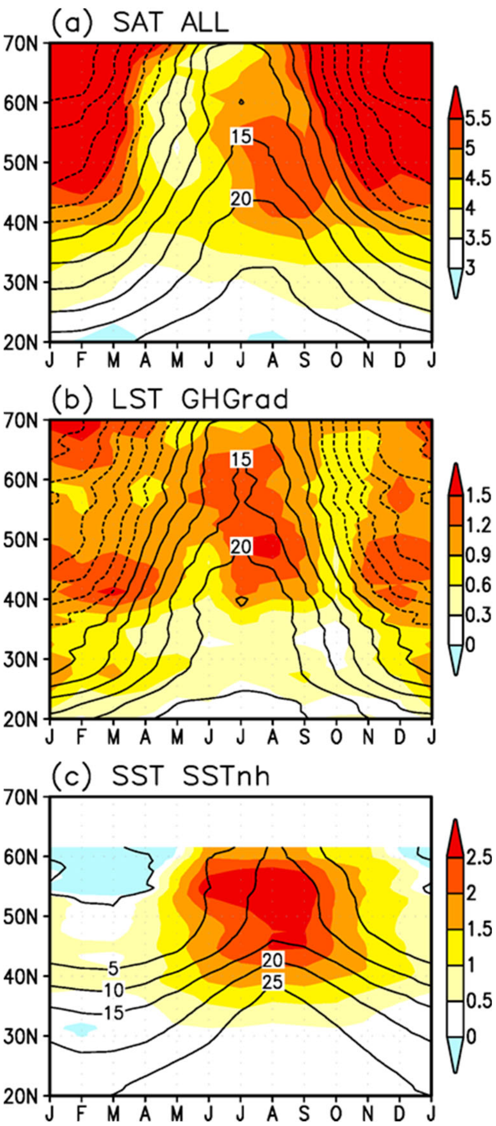
(a) SAT ALL
70N
60N
50N
40N
30N
20N
J F M A M J J A S O N D J
15
20
5.5
5
4.5
4
3.5
3
(b) LST GHGrad
70N
60N
50N
40N
30N
20N
J F M A M J J A S O N D J
15
20
1.5
1.2
0.9
0.6
0.3
0
(c) SST SSTnh
70N
60N
50N
40N
30N
20N
J F M A M J J A S O N D J
5
10
15
20
25
2.5
2
1.5
1
0.5
0

Table 1.

(a) Present-day climate simulations

Run name	Cumulus convection	SST	Period	Ensemble size
HPnn[a]	YS	HadISST1.1	1979–2003	2

(b) Future climate simulations

Run name	Cumulus convection	SST	Period	Ensemble size
HFnn[b]	YS	Each CMIP5 model	2075–2099	28

[a] nn denotes the number of members with different atmospheric initial conditions: nn = 01, 02

[b] nn denotes the number of members with different future SSTs: nn = 01–28

Table 2.

(a) Present-day climate simulations

Run name	Cumulus convection	SST	Period	Ensemble size
HPYSnn[a]	YS	HadISST1.1	1984–2003	2
HPASnn	AS	HadISST1.1	1984–2003	2
HPKFnn	KF	HadISST1.1	1984–2003	2

(b) Future climate simulations

Run name	Cumulus convection	SST	Period	Ensemble size
HFYSC0	YS	CMIP5 MME[b]	2080–2099	1
HFYSC1	YS	CMIP5 cluster 1	2080–2099	1
HFYSC2	YS	CMIP5 cluster 2	2080–2099	1
HFYSC3	YS	CMIP5 cluster 3	2080–2099	1
HFASC0	AS	CMIP5 MME	2080–2099	1
HFASC1	AS	CMIP5 cluster 1	2080–2099	1
HFASC2	AS	CMIP5 cluster 2	2080–2099	1
HFASC3	AS	CMIP5 cluster 3	2080–2099	1
HFKFC0	KF	CMIP5 MME	2080–2099	1
HFKFC1	KF	CMIP5 cluster 1	2080–2099	1
HFKFC2	KF	CMIP5 cluster 2	2080–2099	1
HFKFC3	KF	CMIP5 cluster 3	2080–2099	1

[a] nn denotes the number of members with different atmospheric initial conditions: nn = 01, 02

[b] Multi-model ensemble mean

Table 3.

Run name	Cumulus convection	SST	GHG	Other forcing	Years	Ensemble size[a]
HP	YS	P	P	P	25	3
HF	YS	F	F	F	25	3
Exp1	YS	P	F	P	25	3
Exp2	YS	2.74-K uniform warming over the globe	P	P	25	3
Exp3	YS	F (except for tropics with 2.74-K warming)	F	F	25	3
Exp4	YS	F (except for NH extra-tropics with 2.74-K warming)	F	F	25	3

P: Present-day (1979–2003, observation)

F: Future (2075–2099, RCP8.5)

[a] Ensemble simulation with different initial atmospheric conditions.